JCB Journal of Cell Biology

ARTICLE

Membrane-bound SCF and VCAM-1 synergistically regulate the morphology of hematopoietic stem cells

Jia Hao[1], Hao Zhou[1], Kristen Nemes[1], Daniel Yen[1], Winfield Zhao[1], Charles Bramlett[2], Bowen Wang[2], Rong Lu[1,2,3,4], and Keyue Shen[1,3,5]

Membrane-bound factors expressed by niche stromal cells constitute a unique class of localized cues and regulate the long-term functions of adult stem cells, yet little is known about the underlying mechanisms. Here, we used a supported lipid bilayer (SLB) to recapitulate the membrane-bound interactions between hematopoietic stem cells (HSCs) and niche stromal cells. HSCs cluster membrane-bound stem cell factor (mSCF) at the HSC-SLB interface. They further form a polarized morphology with aggregated mSCF under a large protrusion through a synergy with VCAM-1 on the bilayer, which drastically enhances HSC adhesion. These features are unique to mSCF and HSCs among the factors and hematopoietic populations we examined. The mSCF–VCAM-1 synergy and the polarized HSC morphology require PI3K signaling and cytoskeletal reorganization. The synergy also enhances nuclear retention of FOXO3a, a crucial factor for HSC maintenance, and minimizes its loss induced by soluble SCF. Our work thus reveals a unique role and signaling mechanism of membrane-bound factors in regulating stem cell morphology and function.

Introduction

Adult stem cells are responsible for maintaining and repairing adult tissues and organs and thus a crucial cell source for regenerative medicine. They often reside in specific tissue locations (also known as niches) composed of distinct sets of stromal cells and biomolecules, which support vital stem cell functions, including migration/homing, quiescence, and self-renewal (Ferraro et al., 2010). While adult stem cells can move in and out of their niches (e.g., during transplantation or in response to tissue injury), their physical presence in the niche and localized interactions with surrounding stromal cells are generally required for their long-term functions (Ferraro et al., 2010). It is thus critical to elucidate the key factors and mechanisms underlying these localized stem–stromal interactions.

The membrane-bound factors expressed on stromal cell surfaces constitute a unique class of localized niche cues, which act through direct stem–stromal contact (Lane et al., 2014). Membrane-bound Notch ligands, for example, are involved in stem cell renewal and differentiation in many tissue types (Liu et al., 2010). In the bone marrow niches of hematopoietic stem cells (HSCs), the most-studied and clinically used adult stem cell (Caplan, 2015), several soluble factors exist in the membrane-tethered forms, which work distinctly from their soluble counterparts (Ehninger and Trumpp, 2011). Instead of promoting growth, the membrane-bound stem cell factor (mSCF) is crucial for HSC lodgment, maintenance, and hematopoiesis (Barker, 1994; Driessen et al., 2003), and the membrane-bound version of C-X-C motif chemokine ligand 12 (CXCL12) plays a role in HSC anchorage in the niche rather than chemotaxis (Kollet et al., 2006). Vascular cell adhesion molecule 1 (VCAM-1), a cell–cell adhesion molecule expressed on stromal cells (Jacobsen et al., 1996), regulates HSC homing and retention in the bone marrow (Li et al., 2018; Papayannopoulou et al., 1995). However, it remains unknown on how these membrane-bound factors regulate stem cell behaviors in a localized manner at the cellular level.

Importantly, some membrane-bound factors have shown great promise in enhancing the long-term functions and/or expansion of HSCs ex vivo, the "holy grail" for bone marrow transplantation (Walasek et al., 2012). It has been shown that hematopoietic stem and progenitor cells (HSPCs) cultured on extracellular matrix with immobilized SCF or stromal cells with overexpressed mSCF have improved their maintenance or expansion in vitro (Ajami et al., 2019; Mahadik et al., 2015). Surface-coated fibronectin, which engages very late antigen 4 (VLA-4), the receptor for VCAM-1, also promotes the ex vivo expansion of human HSPCs and mouse HSCs (Feng et al., 2006; Wilkinson et al., 2019). Yet, to date, such applications have been sporadic, with limited success. Further advances in this area demand a mechanistic understanding of the molecular pathways

[1]Department of Biomedical Engineering, University of Southern California, Los Angeles, CA; [2]Department of Stem Cell Biology and Regenerative Medicine, University of Southern California, Los Angeles, CA; [3]Norris Comprehensive Cancer Center, University of Southern California, Los Angeles, CA; [4]Department of Medicine, University of Southern California, Los Angeles, CA; [5]USC Stem Cell, University of Southern California, Los Angeles, CA.

Correspondence to Keyue Shen: keyue.shen@usc.edu.

underlying the membrane-bound factors, their crosstalk with each other, and their downstream targets involved in the long-term functions of HSCs.

The membrane-bound factors in HSC niches have been largely studied with genetic knockdown/knockout or fluorescently tagged models or immunostaining of bone marrow tissues (Acar et al., 2015; Barker, 1994; Ding et al., 2012; Kollet et al., 2006). These in vivo studies provide critical insights on the identity, function, and localization of these factors in the HSC niches. However, no prior knowledge exists on the dynamic molecular and signaling activities in HSCs induced by membrane-bound interactions at the cellular level due to the limits of intravital imaging and the rarity and molecular complexity of the HSC niches (Ehninger and Trumpp, 2011; Morrison and Scadden, 2014). Lately, several in vitro HSC–stromal co-culture studies have demonstrated interesting morphological, migratory, and division patterns of HSPCs physically in contact with stromal cells, which suggests a role of stromal contact for HSC functions (Fonseca et al., 2010; Jing et al., 2010). Yet, whether these cellular behaviors are mediated by specific membrane-bound factors remains unanswered. Other in vitro studies showed adhesive behavior of hematopoietic progenitor cells (HPCs) on substrates with immobilized growth factors (Cuchiara et al., 2013). However, immobilization eliminates the lateral mobility of membrane-bound factors, a crucial property for membrane-bound interactions that allows for micro-/nanoclustering and spatial reorganization of receptors and signaling complexes, which can drastically amplify the membrane-bound signals and achieve distinct cellular functions (Grakoui et al., 1999).

In this study, we used a supported lipid bilayer (SLB) platform to mimic the stromal cell surface and membrane-bound interactions in the context of HSC perivascular niche in the bone marrow (Fig. 1 A). SLB preserves the lateral mobility of membrane-bound proteins and has served as a powerful tool for studying cell–cell interfaces, such as the immunological synapse between T cells and antigen-presenting cells (Grakoui et al., 1999; Manz and Groves, 2010). Here, we demonstrate a unique recruitment pattern and cell morphology taken by HSCs in the interaction with mSCF in the presence of VCAM-1 compared with other membrane-bound factors and HPCs. We further reveal a synergy between mSCF and VCAM-1 in regulating HSC morphology and mSCF recruitment pattern, which dramatically enhances the strength of HSC adhesion on SLB, the degree of which is not seen with multipotent progenitors (MPPs). This synergy involves actin cytoskeleton and phosphatidylinositol 3-kinase (PI3K) signaling, and promotes nuclear FOXO3a retention in contrast to soluble SCF (sSCF). Our work thus reveals a unique role and a new signaling mechanism of membrane-bound factors in mediating stem–stromal interactions, cell adhesion, and stem cell maintenance in the adult stem cell niche.

Results

mSCF is the only factor recruited/clustered by HSCs in a screening

Membrane-bound receptor–ligand engagements often involve recruitment of ligands into microclusters, which precedes downstream cell signaling (Ullrich and Schlessinger, 1990). To determine which membrane-bound factors are recruited/clustered during the HSC–stromal cell interactions, we performed a factor screening using an SLB system (Fig. 1 A), which recapitulates the lateral mobility and dynamic recruitment of the tethered molecules on natural cell membranes (Edidin, 2003). We chose the perivascular niche as the context/background of the factor screening, as most HSCs are found in this niche in the bone marrow (Ding et al., 2012). The chosen ligands include SCF, CXCL12, Ang-1, delta-like 1 (DLL1), and FMS-like tyrosine kinase 3 ligand (Flt3L), which can be found in membrane-bound form in the bone marrow (Arai et al., 2004; Ding et al., 2012; Horiuchi et al., 2009; Kollet et al., 2006; Varnum-Finney et al., 2003), and thrombopoietin (TPO), a systemic, soluble HSC maintenance factor (Decker et al., 2018). These ligands were conjugated with a fluorophore, monobiotinylated, and tethered to the Biotinyl-Cap-PE lipid in the SLBs through a streptavidin "bridge" (Fig. 1 B). VCAM-1 appears abundantly on endothelial cells and leptin receptor–positive ($LepR^+$) mesenchymal stem/stromal cells (MSCs; Ding et al., 2012). We thus included VCAM-1 in all the SLBs in the initial factor screening. VCAM-1 was tethered to the SLBs through the chelation of 6-histidine tail to the DGS-NTA(Ni) lipid for HSC adhesion (Fig. 1 B). We confirmed the lateral mobility and measured the diffusion coefficients of the tethered biomolecules (Fig. S1, A and B). We also confirmed that the density of fluorescent molecules on the SLBs was proportional to the fluorescence intensity (Fig. S1 C), thus allowing for quantitative interpretation of the fluorescence intensity as the number of recruited biomolecules.

FACS was used to sort HSCs ($Lin^-cKit^+Sca1^+Flk2^-CD34^-Slamf1^+$) from the bone marrow of adult mice (4–6 mo old; Fig. S2 A). The freshly isolated HSCs were incubated on SLBs tethered with both VCAM-1 and one of the six screened ligands at 37°C for 1 h and live imaged on an inverted microscope with a heated incubation chamber (37°C). Interference reflection microscopy (IRM) was used to assess the site of cell adhesion on SLBs, with the area and intensity (darkness) indicating the extent and strength of adhesion to the surface (Grakoui et al., 1999; Fig. 1 B). While HSCs adhered to all the bilayers with a screened ligand + VCAM-1, we found that only the membrane-bound SCF (mSCF) was recruited and clustered by HSCs at the HSC–SLB interface (Fig. 1, B and C).

To verify if such recruitment/clustering recapitulates the real HSC-stromal cell interactions in the bone marrow niche, we FACS sorted $LepR^+$ MSCs from the bone marrow (Zhou et al., 2014; Fig. S2 B). The identity of these stromal cells was confirmed by their high mRNA levels of SCF, CXCL12, VCAM-1 and platelet-derived growth factor receptor α (PDGFRα; Fig. S2 C). $LepR^+$ MSCs and HSCs were randomly mixed, incubated for 1 h, fixed, immunostained, and imaged for the heterotypic HSC–$LepR^+$ cell pairs. In ∼80% of HSC–MSC pairs, the mSCF on stromal cells and its receptor, cKit, on HSCs were clustered at the HSC–stromal cell interface, as compared with their diffusive patterns on the individual MSCs and HSCs, respectively (Fig. 1, D and E). Thus, we proceeded with the SLBs to further investigate the HSC–stromal cell interactions mediated through mSCF and VCAM-1 and their downstream signaling activities.

HSCs are highly efficient in recruiting mSCF with a distinct cell morphology

The cKit receptor is expressed on HSCs as well as on MPPs and oligopotent progenitors (OPPs; Shin et al., 2014b), which are

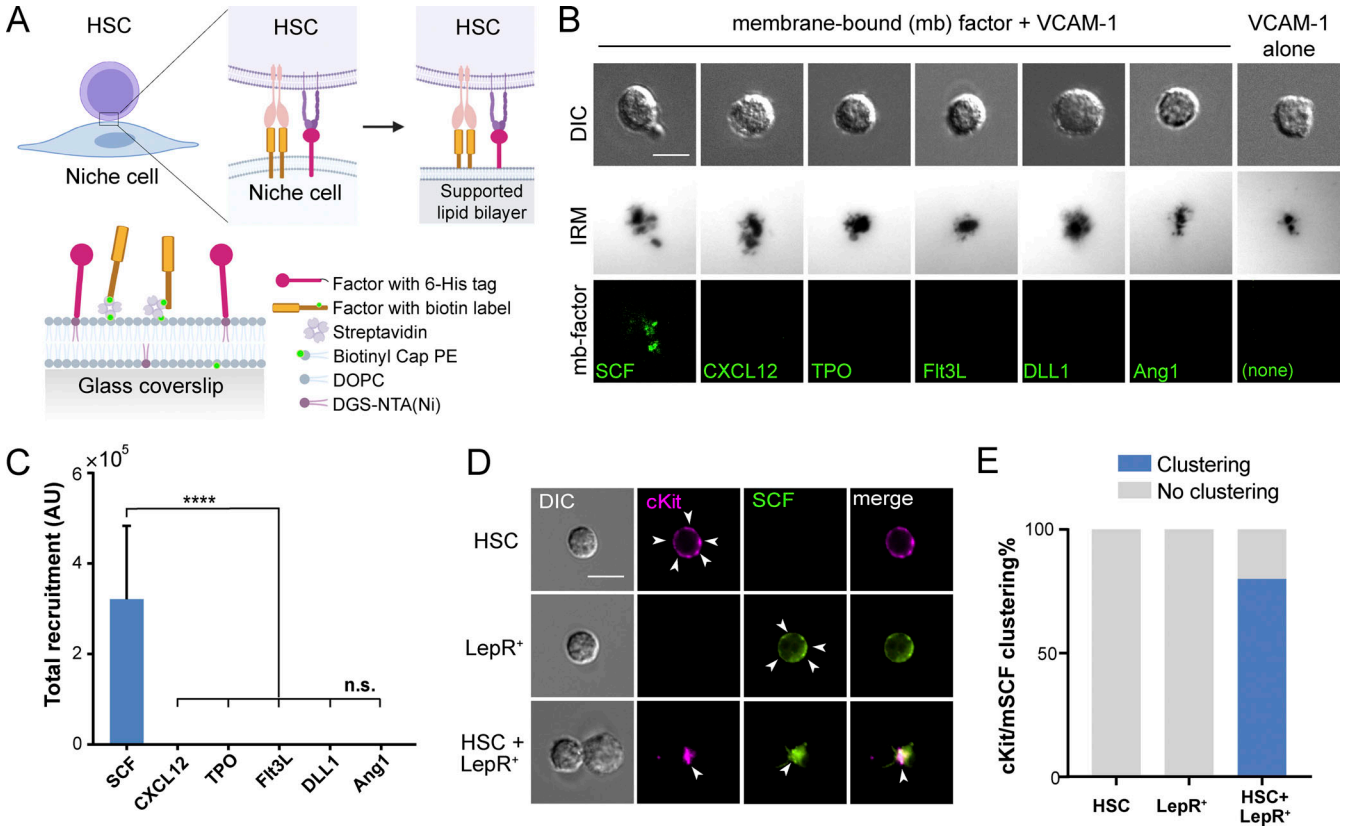

Figure 1. **mSCF is the only factor recruited/clustered by HSCs in a screening. (A)** Illustration of membrane-bound HSC–niche cell interaction and recapitulation on an SLB. **(B)** HSCs after incubation with VCAM-1 and a membrane-bound factor (mb-factor; with fluorescent label, background subtracted) on SLBs for 1 h. DIC, differential interference contrast. Dark regions represent cell–substrate contact/adhesion. Scale bar = 5 µm. **(C)** Total membrane-bound factors recruited by single HSCs assessed by the total fluorescence under each cell. *n* = 37 cells per condition. Error bars represent SD. ****, P < 0.0001 by one-way ANOVA with Tukey's test. AU, arbitrary units. **(D)** HSCs, LepR$^+$ MSCs, and HSC–LepR$^+$ MSC pairs forming physical contact after 1-h incubation. Arrowheads point to dispersed cKit or SCF on the surface of single HSCs or LepR$^+$ MSCs, respectively, or clustered SCF/cKit at the HSC–MSC interface. Scale bar = 5 µm. **(E)** Frequency of cKit/mSCF clustering on one side of the cell in single cells or in HSC–MSC pairs. *n* = 20 single cells or cell pairs for each condition.

believed to be all supported by LepR$^+$ stromal cells (Wei and Frenette, 2018). To investigate whether HSCs and these cKit-expressing progenitors share similar patterns of mSCF recruitment, we FACS sorted HSCs, MPPs (MPP$^-$: Lin$^-$cKit$^+$Sca1$^+$CD34$^+$Flk2$^-$; and MPP$^+$: Lin$^-$cKit$^+$Sca1$^+$CD34$^+$Flk2$^+$), a subset of OPPs (Lin$^-$cKit$^+$Sca1$^-$, which includes the common myeloid progenitor, granulocyte-macrophage progenitor, and megakaryocyte-erythrocyte progenitor), and the lineage-committed bone marrow leukocytes (BMLs; Lin$^+$CD45$^+$ cells, which have no cKit expression and serve as the negative control; Fig. 2 A). cKit expression by the five populations was determined by FACS. Among those, HSCs had an intermediate cKit level between MPPs and OPPs (Fig. 2 A, right panel). Upon incubation on SLBs with mSCF+VCAM-1 at 37°C for 1 h, all the cKit$^+$ cells (HSCs, MPPs, and OPPs) recruited mSCF in clusters at the cell–SLB interface, while the BMLs did not have any detectable mSCF recruitment (Fig. 2 B). Interestingly, HSCs recruited the most mSCF per cell (Fig. 2 C), suggesting that HSCs were more efficient than the MPPs in mSCF recruitment.

Most strikingly, unlike the other cKit$^+$ cells, HSCs often had mSCF clusters polarized to one side of the cell body, which co-localized with distinct large protrusions in the bright field (Fig. 2 B, arrowheads). We first quantified the polarization of mSCF recruitment, defined as the distance between the geometric center of cells in the bright field and the mass center of mSCF clusters (Fig. 2 D, left). HSCs had the most polarized mSCF clusters of all cells, often extending beyond the radii of the cells (~4 µm; Fig. 2 D). Under scanning electron microscopy (SEM), we confirmed that most HSCs indeed had a polarized morphology, with long protrusions extended from the cell body toward one side of the cell beyond the immediate adhesion/contact area on the SLB (Fig. 2 E). The frequency of cells showing distinguishable membrane protrusions (extending from the cell periphery for ≥2 µm) was significantly higher in HSCs (88.0 ± 6.0%) than the more differentiated cells, which ranged from 0% (BMLs) to 13.3% (MPP$^-$), with no statistical differences between them (Fig. 2 F). To assess the stability of the polarized morphology, we cultured HSCs on SLBs with mSCF+VCAM-1 and fixed them at 1, 2, 6, and 12 h. We found that the proportion of HSCs with the polarized morphology remained stable over time (Fig. S3, A and B). Our data indicate that HSCs have a unique interaction pattern with SLBs with mSCF and VCAM-1, which features membrane protrusions and clustering of mSCF at the sites of protrusions.

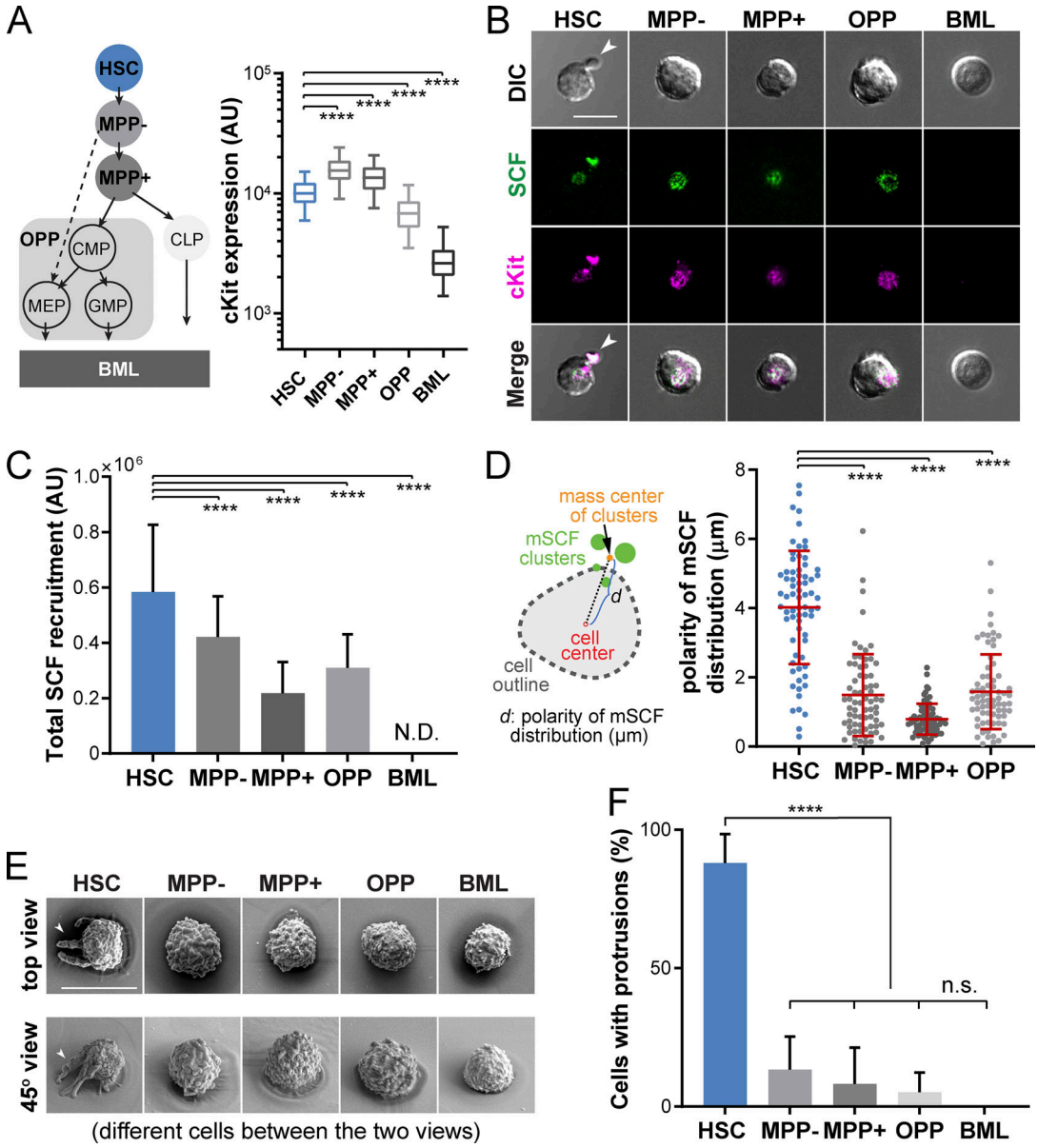

Figure 2. **HSCs are highly efficient in recruiting mSCF with a distinct cell morphology. (A)** Hematopoietic lineage hierarchy and the expression of cKit in five populations measured by flow cytometry (50,000 events in total). MPP⁻: Flk2⁻ MPPs; MPP⁺: Flk2⁺ MPPs; BML, bone marrow Lin⁺CD45⁻ cells. CMP, common myeloid progenitor; GMP, granulocyte-macrophage progenitor; MEP, megakaryocyte-erythrocyte progenitor. **(B)** The clustering patterns of mSCF and cKit under the five hematopoietic cell types after 1-h incubation on SLBs tethered with mSCF+VCAM-1. Arrowheads point to HSCs showing a polarized morphology with mSCF clustered under the cell protrusion. **(C)** Total mSCF per cell recruited by each cell type. *n* = 100–108 single cells per condition. N.D., not detected. **(D)** The polarity of mSCF distribution is defined as the distance between the mass center of mSCF clusters and the cell center. HSCs have the highest polarity of mSCF distribution among all the cKit⁺ HSPCs. *n* = 70 single cells per condition. **(E)** SEM micrographs of the five hematopoietic cells incubated on SLBs with mSCF+VCAM-1. Arrowheads point to HSCs that show unique polarized membrane protrusions (top row, top view; bottom row, 45° side view). **(F)** Frequency of cells with membrane protrusions of 2 µm or longer in SEM. *n* = 3–5 field of views per condition, with 3–10 single cells per field of view. Scale bars, 10 µm. Error bars represent SD. ****, P < 0.0001 by ANOVA with Tukey's test.

VCAM-1 promotes polarized morphology and mSCF recruitment pattern in HSCs

We next investigated the contributions of mSCF and VCAM-1 in forming the polarized HSC morphology and mSCF recruitment pattern. Freshly isolated HSCs were incubated for 1 h on SLBs with VCAM-1 or mSCF alone, or with both factors (mSCF+VCAM-1), and examined for their adhesion and morphology with light microscopy and SEM (Fig. 3 A). With VCAM-1 alone, HSCs had a noncharacteristic, rounded morphology in the bright field and formed continuous contact with the SLB in IRM (Fig. 3 A), the area of which was slightly larger than those on a blank SLB (Fig. S3, C and D). In contrast, HSCs on mSCF-alone SLB were featured with small multifocal adhesion footprints in IRM. When both mSCF and VCAM-1 were present, the polarized morphology emerged, with distinct protrusions toward one side of the cell body (Fig. 3 A). Strikingly, under SEM,

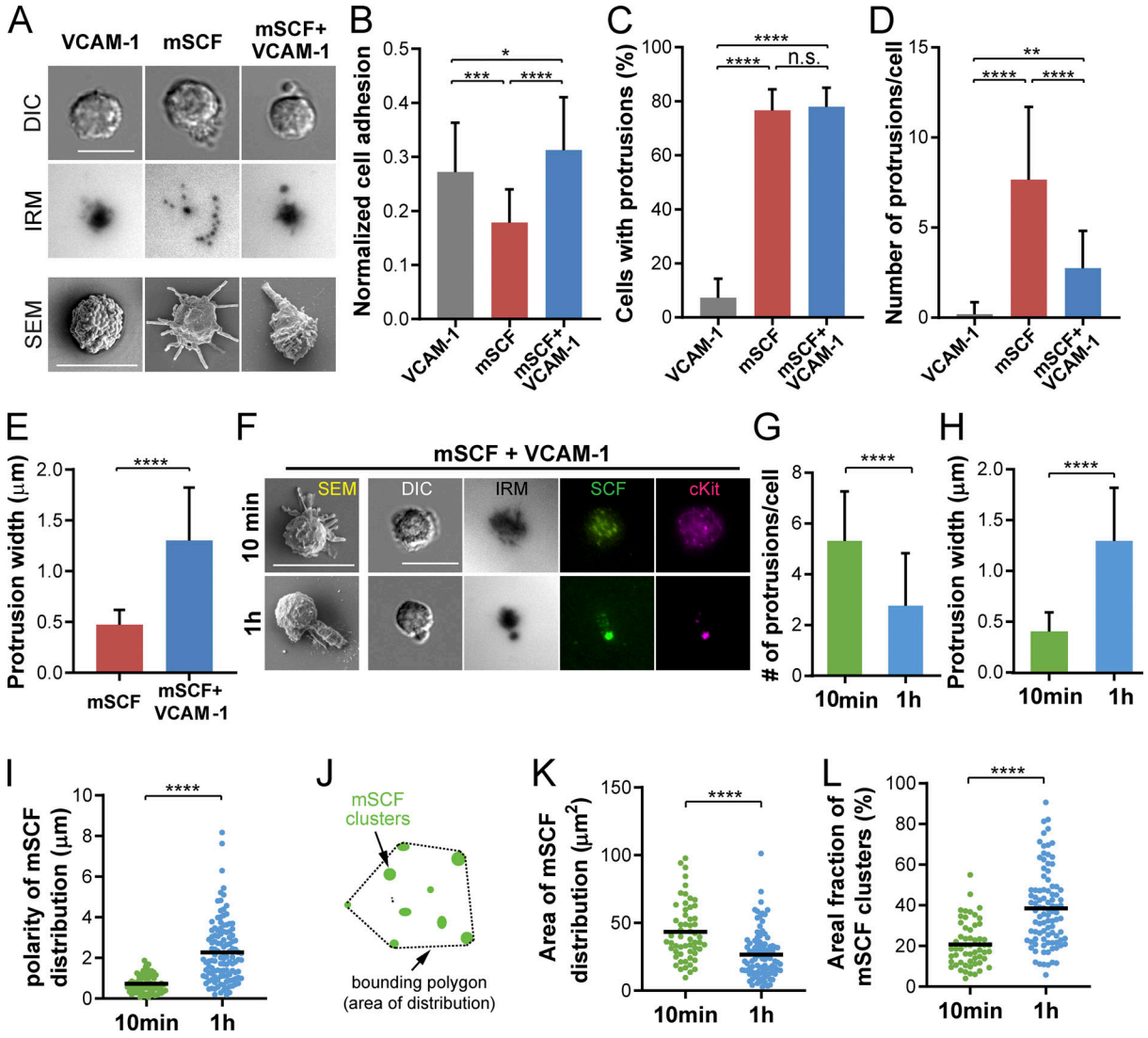

Figure 3. **VCAM-1 promotes polarized morphology and mSCF recruitment pattern in HSCs. (A)** DIC, IRM, and SEM images of HSCs after 1-h incubation on SLBs with VCAM-1 alone, mSCF alone, or mSCF+VCAM-1. **(B)** Comparison of normalized cell adhesion areas in microscopy (adhesion measured in IRM divided by cell area measured in DIC). *n* = 21–83 cells per condition. **(C–E)** Analyses of HSC morphology from SEM images. **(C)** Frequency of cells showing membrane protrusions ≥ 2 µm in SEM. *n* = 3 SEM area per condition with 20–40 single cells per area. **(D)** Number of protrusions ≥2 µm per cell in SEM. *n* = 20–30 single cells per condition. **(E)** Width of protrusions measured at the middle point. *n* = 30–82 single cells per condition. **(F)** SEM and microscopic images of HSCs incubated on mSCF+VCAM-1 SLBs for 10 min and 1 h. **(G and H)** Corresponding quantifications of number of membrane protrusions per cell (G) and average width of membrane protrusions under SEM (H). *n* = 18 (10 min) and *n* = 30 (1 h) single cells per condition. **(I)** Polarity of recruited mSCF by HSCs. *n* = 74 (10 min) and *n* = 120 (1 h) single cells per condition. **(J)** Definition of the area of mSCF distribution. **(K and L)** Quantification of area of mSCF distribution (K) and percentage of area occupied by mSCF clusters in the total area of mSCF distribution (L). *n* = 57 (10 min) and *n* = 94 (1 h) single cells per condition. Scale bars, 10 µm. Error bars represent SD. *, P < 0.05; **, P < 0.01; ***, P < 0.001; ****, P < 0.0001 by ANOVA with Tukey's test (B–D) and two-tailed unpaired Student's *t* test (E, G–I, K, and L).

cells on VCAM-1 alone had little or no protrusions from their surface; with mSCF alone, slim protrusions could be observed pointing in all directions, as opposed to the large, polarized protrusion seen with mSCF+VCAM-1 (Fig. 3 A, bottom). We found that the normalized cell adhesion, defined as the adhesive area in IRM divided by the cell area in the bright field, was the lowest with mSCF alone while being similar between the VCAM-1 –containing conditions, demonstrating a role of VCAM-1 in promoting HSC adhesion. Quantitative analysis of the SEM images shows that HSCs had minimal protrusions on SLB with VCAM-1 alone, measured by both the percentage of cells with protrusions ≥2 µm in length and the number of such protrusions per cell (Fig. 3, C and D). Interestingly, mSCF was sufficient to induce cell protrusions in HSCs with or without VCAM-1 (Fig. 3 C), while the number of protrusions per cell was reduced (Fig. 3 D) and their width increased (Fig. 3 E) by the presence of VCAM-1. The data here suggest that the large protrusion and polarized morphology are synergistically induced by VCAM-1 and mSCF.

Notably, the number of protrusions per cell and the protrusion width were negatively associated in the mSCF and mSCF+VCAM-1 conditions (Fig. 3, D and E). We hypothesized that the polarized morphology of HSCs on mSCF+VCAM-1 was preceded in time by

a multifocal morphology similar to that with mSCF alone. To test the hypothesis, we examined HSCs on SLBs with mSCF+VCAM-1 fixed after 10-min or 1-h incubation (Fig. 3 F). The HSC morphology on mSCF+VCAM-1 SLBs at 10 min indeed resemble that on mSCF-alone SLBs at 1 h. Importantly, the number of protrusions (≥2 µm) per cell reduced significantly after 1 h of incubation (Fig. 3, F and G), while their average width more than doubled from <0.5 µm to >1.2 µm (Fig. 3 H). The polarity of mSCF distribution also increased significantly over time (Fig. 3, F and I). In addition, we noted a transition in the distribution of mSCF clusters from a diffused, multifocal pattern to a more concentrated one (Fig. 3 F). This was confirmed by measuring the distribution of mSCF clusters (Fig. 3 J), which features a reduction of total area of mSCF distribution (Fig. 3 K) and an increase of areal fraction of mSCF clusters within the distribution area (Fig. 3 L). With time-lapse microscopy, we further observed that early on, HSCs gained more adhesion and mSCF recruitment in a smaller footprint on mSCF+VCAM-1 SLBs than those on mSCF alone surfaces over time (Fig. S4, A–E). Overall, our data here indicate that VCAM-1 dynamically and synergistically regulates the morphology of HSCs and the interaction pattern of HSCs with mSCF and promotes a more polarized, clustered distribution of mSCF recruitment.

mSCF and VCAM-1 synergistically promote HSC adhesion

Cell adhesion is crucial for HSC homing and maintenance in the niche (Chen et al., 2013). The increased normalized adhesion area of HSCs on mSCF+VCAM-1 SLB (Figs. 3 B and S4 B) suggest a stronger cell–SLB interaction under the mSCF–VCAM-1 synergy. To measure the strength of such interaction/adhesion, we designed a microfluidic device that imposes controlled shear stresses on the adhered HSCs (Fig. 4 A). HSCs and MPP^- cells were loaded and incubated in the device for 1 h to establish the adhesion on pairs of SLB surfaces, respectively (HSCs in Fig. 4 B). As a measure of the adhesion strength, we interpolated the flow rates at which 50% of the cells were peeled off and calculated the corresponding flow shear stresses at the SLB surface (Fig. 4, C and D). We found that mSCF alone provided little strength in cell adhesion, while VCAM-1 alone provided similar, intermediate adhesive strength to both HSCs and MPPs. In contrast, mSCF+VCAM-1 dramatically increased the adhesion of HSCs by 50-fold from those on VCAM-1 alone (Fig. 4 C) compared with a fivefold increase on mSCF+VCAM-1 versus VCAM-1 for MPP^- cells (Fig. 4 D), the progenitor closest to HSCs in the lineage hierarchy (Fig. 2 A). Notably, we did not see a synergistic effect of SCF and VCAM-1 on HSC adhesion when the two were directly immobilized on the glass (Fig. S4, F and G), where HSCs had similar adhesion on all the three surfaces under a high flow rate (15 ml/min) that would peel most HSCs off SLBs (Fig. 4 C).

We further investigated the role of the polarized morphology in HSC adhesion on the mSCF+VCAM-1 SLBs. Under 60× magnification, we observed that HSCs remained largely unchanged under most flow rates (low to medium). Under a high flow rate (11 ml/min), the adhesion and orientation of the remaining cells started to change, albeit mildly. We defined the protrusion angle (θ; 0° to ∼180°) as the angle between the flow direction and the cell-to-protrusion vector in HSCs (Fig. 4 E). Under the 11-ml/min flow rate, HSCs had significant changes in θ compared with the no-flow condition (Fig. 4 F). Further examination revealed that those with cell bodies upstream of the protrusions (i.e., $\theta < 90°$; Fig. 4 E, top row) would reorient the cell bodies more to the downstream (i.e., larger $\Delta\theta$), while those with cell bodies already at the downstream ($\theta > 90°$, Fig. 4 E, bottom row) often had a slight extension of the protrusion without much change in θ (Fig. 4 G). In both cases, the protrusion remained anchored while the cell body shifted. These findings suggest that the protrusions formed a stronger adhesion on SLBs than the cell body. Overall, our results here demonstrate a distinct functional role of the mSCF and VCAM-1 synergy and the polarized morphology in promoting HSC adhesion.

mSCF redistribution and morphological transition require cytoskeletal remodeling

We next investigated the involvement of cytoskeletal components in shaping the HSC morphology under the mSCF–VCAM-1 synergy. It was previously shown that microcluster recruitment by T cells during the formation of immunological synapse require actin polymerization and myosin contraction (Dustin, 2007). In human HSPCs, myosin IIa and IIb are further differentially regulated in cell polarization (Shin et al., 2014a). We first examined the subcellular distribution of F-actin, myosin IIa, and myosin IIb in mouse HSCs with the polarized morphology on mSCF+VCAM-1 SLBs (Fig. 5 A). Notably, F-actin and myosin IIa were more specifically enriched at the protrusion. Myosin IIa also appeared more cortical than myosin IIb, the latter of which was relatively uniformly distributed across the cell (Fig. 5 B), suggesting more involvement of F-actin and myosin IIa than myosin IIb in the peripheral reorganization of protrusions. To understand their roles in forming the polarized morphology, we next treated HSCs upon seeding on mSCF+VCAM-1 SLBs with inhibitors of myosin contraction (with blebbistatin [Blebb]), actin polymerization (with latrunculin A), and Rho-associated protein kinase (ROCK; with Y27632) for 1 h before fixation and downstream analyses (Fig. 5 C). All three drugs prevented the polarized morphology of HSCs while resulting in different morphological characteristics (Fig. 5 D). Latrunculin A abrogated almost all the protrusions from the cell surface, resulting in a smooth, "dough"-like morphology. Blebb did not fully disrupt membrane protrusions but led to long, slim ones pointing in all directions (Fig. 5 D). Those treated with ROCK inhibitor Y27632 had spiky protrusions shorter than those under the DMSO and Blebb conditions (Fig. 5, D and F). Importantly, while HSCs still formed tiny mSCF clusters on SLBs (and cKit clusters on cell membrane), their ability to make large mSCF and cKit clusters in polarized, tight distribution was impaired by all three inhibitors (Fig. 5, E, G, and H). Interestingly, all inhibitions except for ROCK inhibition (Fig. S5 A) led to minor changes in the normalized cell adhesion area, while the total mSCF recruitment was not impacted (Fig. S5 B). These results indicate that the actomyosin cytoskeleton and ROCK activity play a primary role in forming large protrusions and polarized/tightly distributed mSCF in the mSCF–VCAM-1 synergy but are not required for enhancing the total mSCF recruitment.

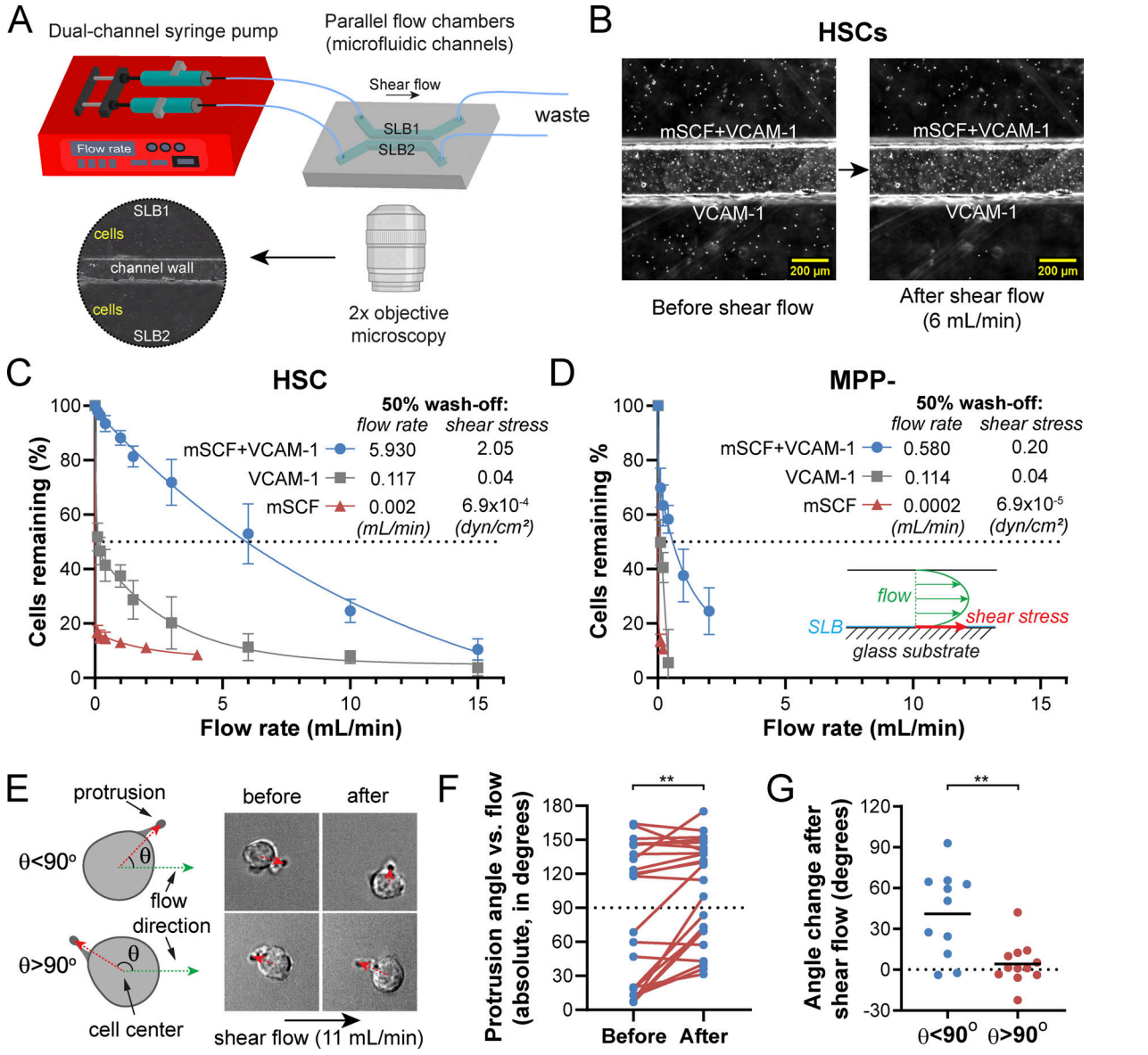

Figure 4. **mSCF and VCAM-1 synergistically promote HSC adhesion. (A)** Microfluidic setup for assessing the strength of HSC adhesion to SLBs tethered with membrane-bound factors. **(B)** 2× bright-field images of HSCs seeded on SLBs with mSCF+VCAM-1 and VCAM-1 alone, respectively. Before shear flow (left) and after the shear flow of 6 ml/min (right). **(C and D)** Percentages of HSCs (C) and MPP⁻ cells (D) remaining on the SLBs after a series of increasing flow rates and the 50% wash-off flow rates and corresponding shear stresses on SLBs. *n* = 5 ROIs per data point. **(E–G)** Effect of shear flow on the orientation of the HSC protrusions on the SCF+VCAM-1 SLBs. **(E)** Definition of the protrusion angle (θ) and orientation changes in HSCs with different starting θ before and after the shear flow (11 ml/min). **(F)** Protrusion angles of single HSCs before and after the shear flow. **(G)** Changes of protrusion angles ($\theta_{after} - \theta_{before}$) in HSCs with starting θ greater or less than 90°. *n* = 22 single HSCs. Error bars represent SD. **, P < 0.01 by paired Student's *t* test and unpaired two-tailed Student's *t* test in F and G, respectively.

mSCF–VCAM-1 synergy involves PI3K signaling

Both mSCF/cKit and VCAM-1/VLA-4 engagements have been reported to activate PI3K signaling (Alexeev and Yoon, 2006; Matsunaga et al., 2003), which is upstream of cytoskeletal remodeling and ROCK activity (Figs. 5 C and 6 A). We thus investigated the involvement of PI3K in the mSCF–VCAM-1 synergy in HSCs. HSCs were fixed after incubation on SLBs with mSCF alone or mSCF+VCAM-1 for 15 min or 1 h and immunostained for intracellular PI3K. Using total internal reflection fluorescence (TIRF) microscopy, we found that PI3K was predominantly colocalized with cKit/mSCF clusters (Fig. 6 B). Importantly, despite of an overall decrease of the colocalization over time in both conditions, the PI3K/cKit colocalization was independent of the presence of VCAM-1 (Fig. 6 C), suggesting cKit as the major site of intracellular PI3K recruitment.

PI3K activation during VCAM-1 engagement has been shown to phosphorylate the protein kinase Akt (Matsunaga et al., 2003; Fig. 6 A). We next investigated the role of the three sequential signaling steps (i.e., VCAM-1 engagement, PI3K activation, and Akt phosphorylation) in the formation of the distinct mSCF recruitment pattern and HSC morphology. We first used the small-molecule inhibitors BIO5192 (BIO) to disrupt the interaction of

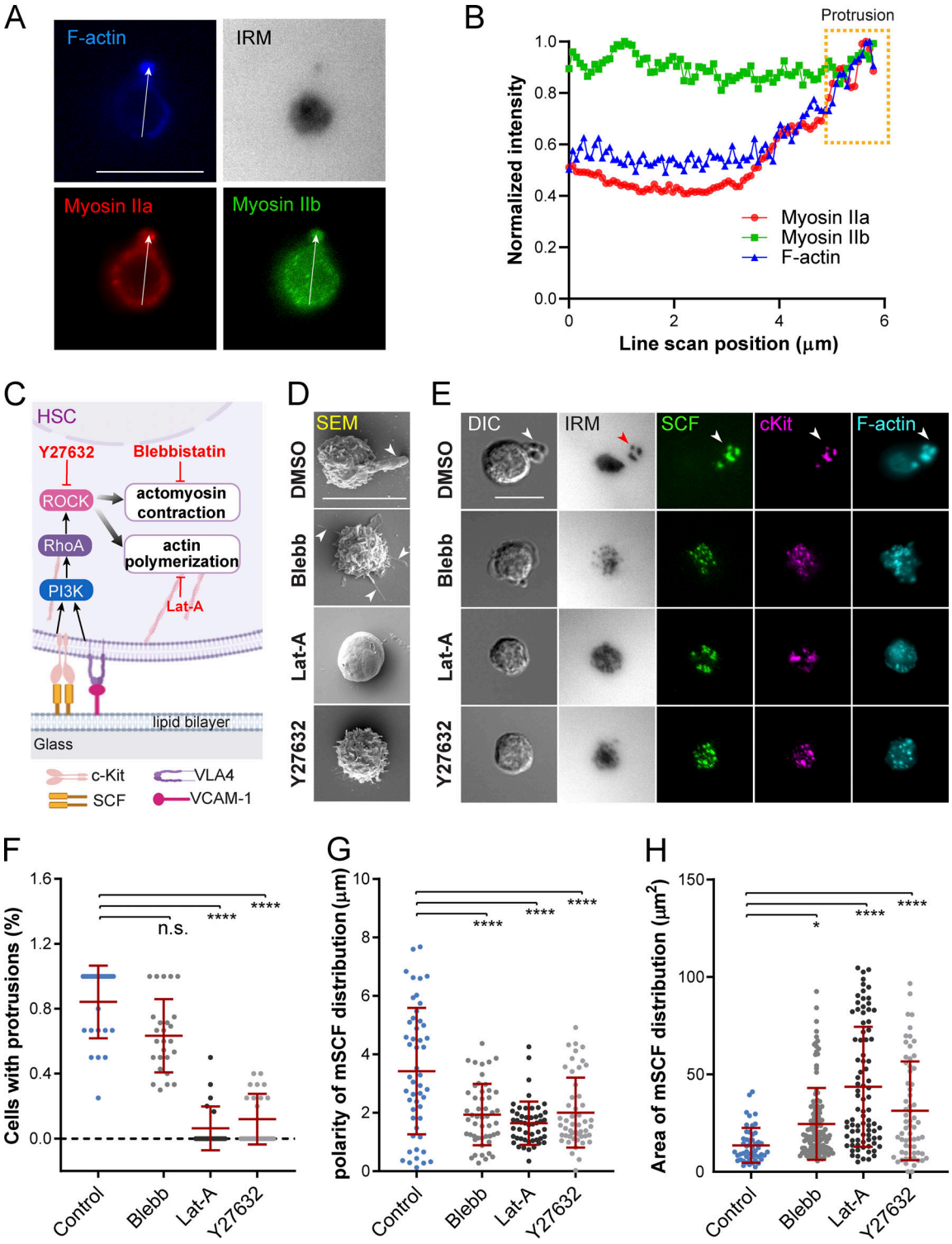

Figure 5. **mSCF redistribution and morphological transition require cytoskeletal remodeling. (A)** Immunostaining of myosin IIa and myosin IIb and counterstained F-actin in an HSC forming polarized morphology on an SLB with mSCF+VCAM-1. **(B)** Line scan of fluorescent intensities of the three cytoskeletal components as illustrated in A. The yellow box highlights the region of the protrusion. **(C)** ROCK signaling and cytoskeletal reorganization downstream of mSCF and VCAM-1 engagement and the corresponding inhibitors. **(D)** SEM images of HSCs pretreated with inhibitors for 1 h and then incubated with SLBs with mSCF+VCAM-1 for 1 h. Arrowheads indicate protrusions on HSCs. **(E)** Microscopic images of HSCs from the corresponding treated or nontreated conditions in D. Arrowheads (white and red) show colocalization of membrane protrusion with adhesion sites and clusters of cKit, mSCF, and F-actin. **(F)** Frequency of cells showing membrane protrusions ≥2 µm in SEM. *n* = 23–26 cells per condition. **(G)** Polarity of mSCF distribution under single HSCs. *n* = 50 cells per condition. **(H)** Area of the mSCF distribution under single HSCs. *n* = 59–84 single cells per condition. Scale bars, 10 µm. Error bars represent SD. *, $P < 0.05$; ****, $P < 0.0001$ by ANOVA with Tukey's test (F–H).

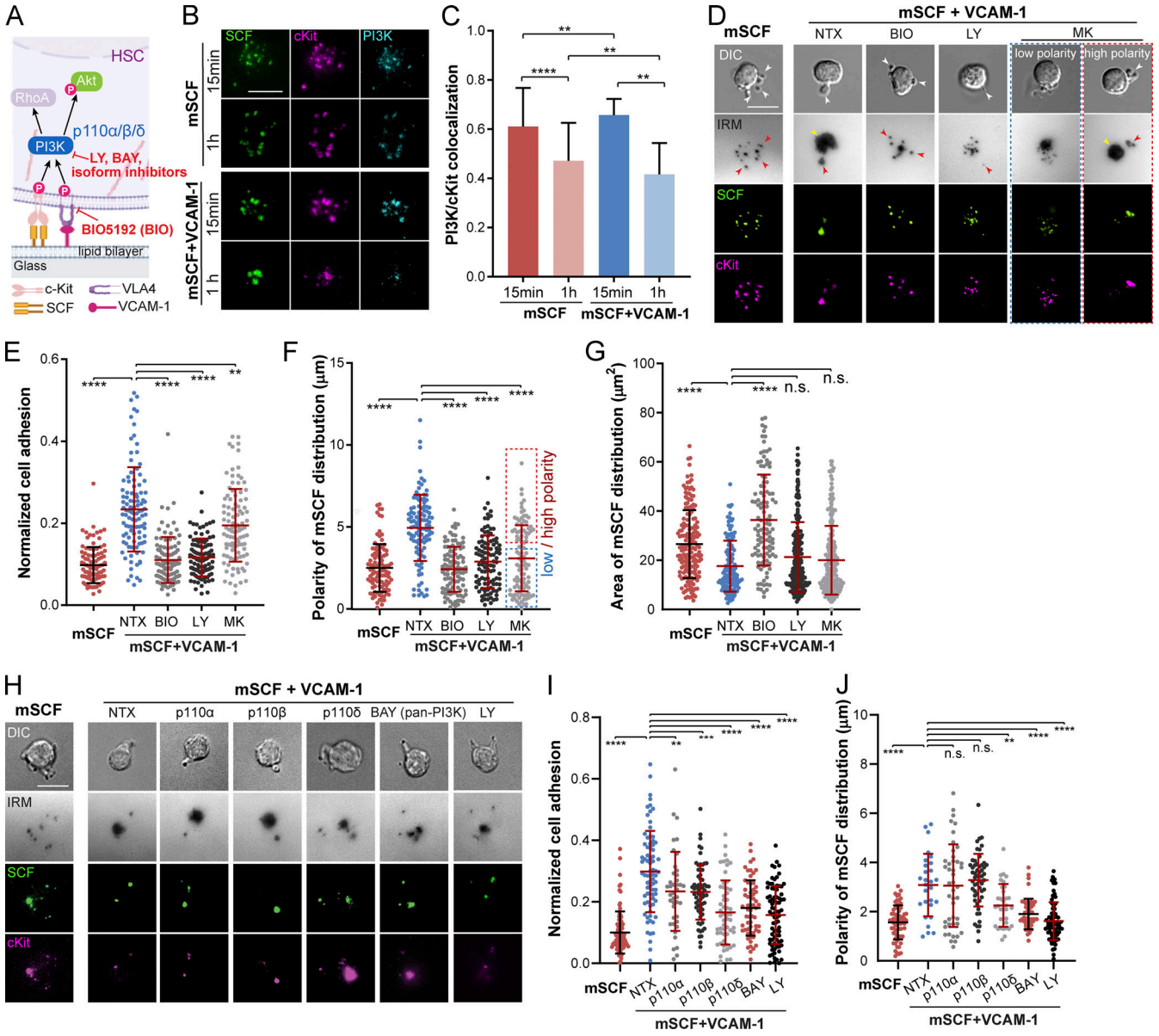

Figure 6. **mSCF–VCAM-1 synergy involves PI3K–Akt signaling. (A)** PI3K–Akt signaling downstream of HSC engagement with mSCF and VCAM-1 and the corresponding inhibitors. **(B)** TIRF images of PI3K immunostaining in HSCs after 15-min or 1-h incubation on SLBs with mSCF or mSCF+VCAM-1. Scale bar, 5 µm. **(C)** Colocalization of PI3K and cKit. *n* = 20 single cells per condition. **(D)** Microscopic images of HSCs on SLB with mSCF alone (nontreated) or the nontreated and drug treated conditions on SLBs with mSCF+VCAM-1. White arrowheads show protrusions visible in the bright field, yellow arrowheads show adhesion under cell body, and red arrowheads show adhesion through elongated protrusions. **(E–G)** Corresponding quantifications of normalized cell adhesion (E), polarity of mSCF distribution (F), and area of mSCF distribution (G). **(E and F)** *n* = 100–104 single cells per condition. **(H–J)** HSCs on SLBs under pan- and isoform-specific PI3K inhibitions (H), and the quantifications of normalized cell adhesion (I) and polarity of mSCF distribution (J). **(I and J)** *n* = 41–91 single cells per condition. **(D and H)** Scale bars, 10 µm. Error bars represent SD. **, P < 0.01; ***, P < 0.001; ****, P < 0.0001 by ANOVA with Tukey's test (C, E–G, I, and J).

VCAM-1 with VLA-4 and LY294002 (LY) and MK2206 (MK) to inhibit PI3K activation and Akt phosphorylation, respectively. Nontreated HSCs were incubated on SLBs with mSCF alone or mSCF+VCAM-1 as controls. Consistent with the earlier findings (Fig. 3 A), incubation of HSCs with mSCF alone resulted in multiple membrane protrusions (white arrows) and multifocal adhesion with lipid bilayer (red arrows) at the site of cKit/mSCF clusters (Fig. 6 D). The presence of VCAM-1 promoted extended adhesion with a polarized morphology of the cell (Fig. 6 D), which was completely disrupted by BIO and LY and partially by MK (Fig. 6, D and E). All three inhibitions significantly reduced the polarity of mSCF distribution (Fig. 6 F), yet under MK, there were more residual polarized HSCs similar to the untreated ones (Fig. 6, D and F, red box). Moreover, only the BIO treatment led to a significant increase of the area of mSCF distribution (Fig. 6 G). Inhibiting Akt with an alternative, GSK2141795 (or Uprosertib) had similar effects to MK (Fig. S5, C–F). These results suggest that while all three signaling steps (VLA4–PI3K–Akt) are involved in the cell adhesion and the polarity of mSCF distribution, the redistribution of mSCF on SLBs is primarily regulated by

VCAM-1–mediated adhesion. The differential results of Akt and PI3K inhibitions also implies an involvement of downstream targets other than Akt in VCAM-1 and PI3K activation.

LY was reported to also target bromo- and extra-terminal domain family proteins (Dittmann et al., 2014). Meanwhile, among the eight isoforms of PI3K, class IA PI3Ks are involved in the signaling directly downstream of membrane-bound receptors (Bilanges et al., 2019). Hematopoietic cells express three isoforms of the p110 subunit of the class IA PI3Ks, the p110α, β, and δ (Hemmati et al., 2019). To rule out the off-target effect of LY and determine which of the three PI3K isoforms are primarily involved in the mSCF–VCAM-1 synergy, we treated HSCs with another pan-PI3K inhibitor, BAY 80-6946 (BAY), and three isoform-specific inhibitors to p110α (MLN1117), p110β (TGX-221), and p110δ (CAL-101), respectively. All four inhibitors resulted in a decrease of HSC adhesion on SLBs with mSCF+VCAM-1, with p110δ and pan-PI3K (BAY) inhibitions causing greater disruptions and resulting in a multifocal footprint (Fig. 6, H and I). We also noticed that inhibiting p110δ, but not p110α or p110β, led to a significant reduction in the polarity of mSCF distribution (Fig. 6 J) to a level like the BAY treatment. Our findings here thus confirm the role of PI3K and indicate the p110δ isoform as the major player in regulating the adhesion and formation of the polarized mSCF distribution in the mSCF–VCAM-1 synergy.

mSCF–VCAM-1 synergy promotes nuclear FOXO3a retention

Next, we examined the effect of the mSCF–VCAM-1 synergy on downstream signaling and nuclear FOXO3a (Fig. 7 A). SCF can activate cKit phosphorylation to initiate PI3K/Akt signaling (Mazzoldi et al., 2019). We examined the colocalization of mSCF/cKit clusters with all phosphorylated tyrosine residues (pY) by immunostaining and TIRF microscopy (Fig. 7 B). The pY staining was found largely colocalized with SCF/cKit clusters without or with VCAM-1 (Fig. 7 B, top two rows). Importantly, the presence of VCAM-1 promoted tight clustering of pY staining and its colocalization with cKit, which can be reverted by VCAM-1 inhibition through BIO pretreatment (Fig. 7, B and C). Our result suggests that VCAM-1 promotes the tyrosine phosphorylation that directly associates with cKit in HSCs.

FOXO3a is a transcription factor that plays an important role in maintaining the HSC pool through activities in nucleus (Miyamoto et al., 2007). We next studied the effects of the mSCF–VCAM-1 synergy on nuclear retention of FOXO3a in HSCs. HSCs were incubated on SLBs with mSCF with or without VCAM-1 for 12 h and immunostained for FOXO3a. We found that HSCs on mSCF+VCAM-1 SLBs had significantly higher nuclear FOXO3a compared with those on mSCF alone (Fig. 7, D and E). In addition, pretreatments of HSCs with the VCAM-1 and PI3K inhibitors (BIO and LY) reduced nuclear FOXO3a levels (Fig. 7, D and E). In contrast, pretreatment of HSCs with the Akt inhibitor MK further promoted the nuclear FOXO3a level compared with the nontreated group (Fig. 7, D and E). We further examined the effects of the p110α, p110β, and p110δ isoform-specific PI3K inhibitors (the same ones used in Fig. 6, H–J). The nuclear FOXO3a levels were significantly reduced by pan-PI3K inhibition (by BAY and LY), but not the individual isoform inhibitors (Fig. 7 G), indicating a functional redundancy among the three isoforms for nuclear FOXO3a regulation. While the effect of Akt inhibition on nuclear FOXO3a is expected, the result of PI3K inhibition was contrary to the known negative regulation of nuclear FOXO3a by the PI3K–Akt pathway, suggesting a previously unknown, positive role of PI3K in promoting the maintenance of nuclear FOXO3a through the mSCF–VCAM-1 synergy.

sSCF competitively disrupts mSCF–VCAM-1 synergy

sSCF is an essential growth factor commonly used in HSC cultures for their maintenance and proliferation (Eaves et al., 1997). Since both the soluble and membrane-bound forms of SCF can engage cKit, we next investigated the role of sSCF in the mSCF–VCAM-1 synergy in HSCs. HSCs were incubated with sSCF before (pre-TX) or 30 min after (post-TX) being seeded onto mSCF+VCAM-1 SLBs. We found that the pre-TX HSCs recruited significantly less mSCF compared with those without sSCF (nontreated); in contrast, the post-TX HSCs retained the mSCF recruitment (Fig. 8, A and B). This suggests that both sSCF and mSCF can occupy and prevent the other from binding to cKit. Cell adhesion was found slightly impaired by sSCF under both treatment conditions, with more disruption in the pre-TX group (Fig. 8 C). Importantly, we observed a striking difference in cell morphology with the pre-TX HSCs, which barely formed any membrane protrusions (Fig. 8, A and D). Such morphological disruption in the pre-TX HSCs coincided with a loss of polarization and widened area of mSCF distribution compared with the nontreated condition (Fig. 8, E and F). In contrast, the post-TX cells largely retained the polarized morphology with a large, distinct protrusion, with minimal changes in the overall distribution of mSCF clusters on SLBs (Fig. 8, E and F).

Next, we examined the downstream effect of sSCF on the maintenance of nuclear FOXO3a by the mSCF–VCAM-1 synergy (Fig. 7, D and E). We extended the incubation of HSCs on mSCF+VCAM-1 SLBs without or with pre- or posttreatment of sSCF to 12 h before fixation and immunostaining for FOXO3a and compared the results to HSCs incubated with mSCF or sSCF alone (Fig. 8 G). We found that the presence of sSCF impaired the maintenance of nuclear FOXO3a in HSCs by the mSCF–VCAM-1 synergy, while the difference between pre- and post-TX was not significant (Fig. 8 H). Strikingly, even with sSCF, the nuclear FOXO3a levels remained significantly higher in HSCs on the mSCF+VCAM-1 SLBs than those treated with sSCF alone (Fig. 8 H). Overall, the data here suggest a competitive/disruptive nature of sSCF against mSCF for cKit engagement and morphological regulation and the ability of mSCF to promote nuclear FOXO3a maintenance despite the presence of sSCF (Fig. 8 I).

Discussion

Membrane-bound factors have long been recognized as a crucial component in HSC niches in the bone marrow (Crane et al., 2017). However, little is known about how HSCs interact with membrane-bound factors and how these localized interactions in the niches contribute to HSC phenotype/cellular activities at the single-cell level. Here, we reported a clustered recruitment pattern and a polarized morphology assumed by HSCs in the

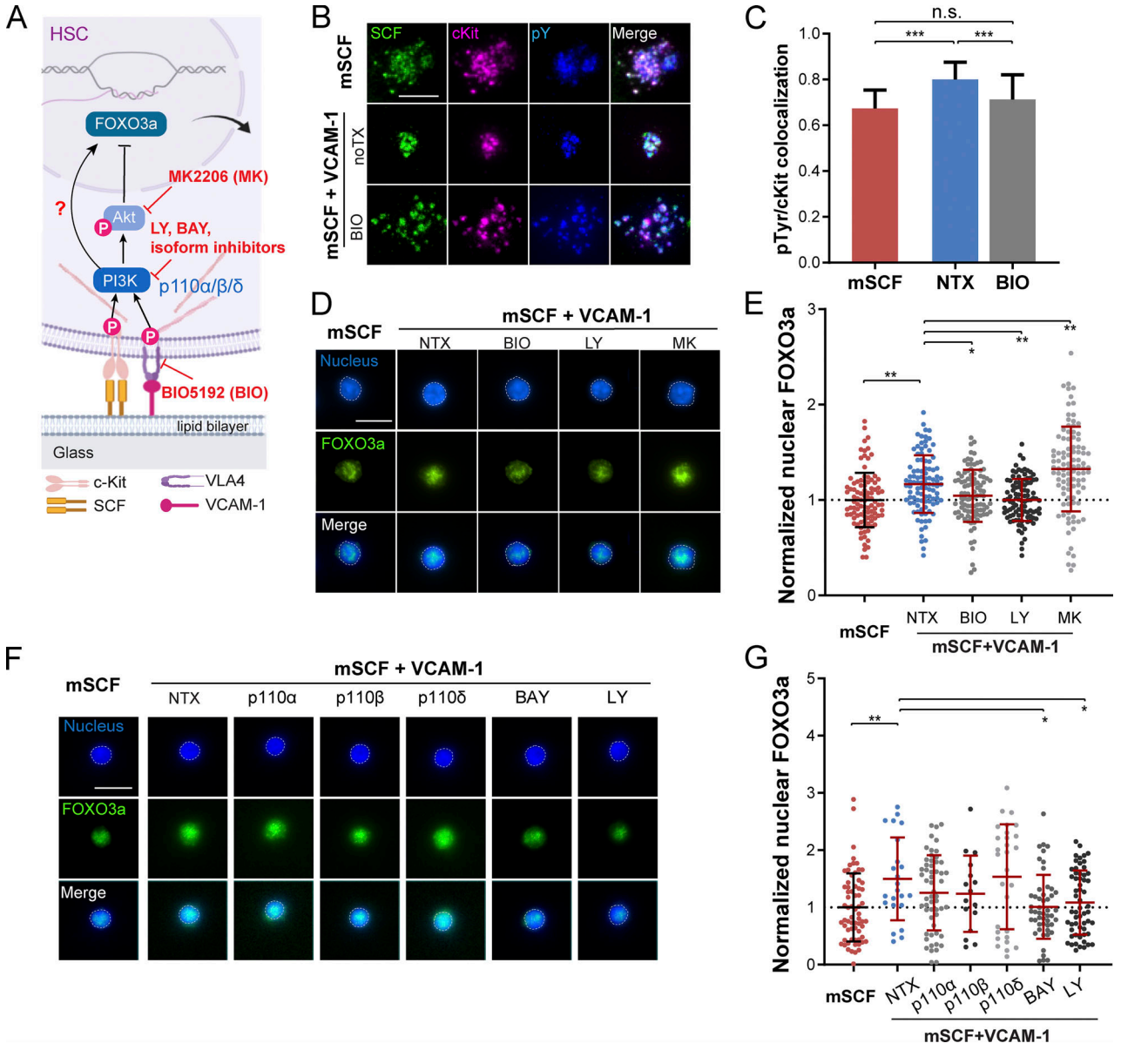

Figure 7. **mSCF–VCAM-1 synergy promotes nuclear FOXO3a retention. (A)** PI3K–FOXO3a signaling in HSCs in an Akt-dependent or independent manner upon engagement with mSCF and VCAM-1. **(B)** TIRF microscopy images of phosphorylated tyrosine residue (pY) immunostaining (with 4G10) in HSCs after 1-h incubation on SLBs with mSCF alone or mSCF+VCAM-1 without or with preinhibition of VLA-4 for 1 h. Scale bar, 5 µm. **(C)** Colocalization of pY and cKit clusters under the three conditions. *n* = 9–41 single cells per condition. **(D)** FOXO3a immunostaining (nuclei counterstained) of HSCs incubated for 12 h on SLBs with mSCF alone or mSCF+VCAM-1 without or with VLA-4, PI3K, and Akt inhibitors. **(E)** Intensities of nuclear FOXO3a immunostaining in single HSCs, normalized to the population average of the mSCF-alone condition. *n* = 100 single cells per condition. **(F and G)** FOXO3a immunostaining of HSCs incubated for 12 h on SLBs with mSCF alone or mSCF+VCAM-1 without or with pan- and isoform-specific PI3K inhibitors (F), and corresponding quantification of intensities of nuclear FOXO3a immunostaining (G), normalized to the population average of the mSCF-alone condition. *n* = 16–66 single cells per condition. **(D and F)** Dashed lines show contour of nuclei used for nuclear FOXO3a quantification. Scale bars, 10 µm (D and F). Error bars represent SD. *, P < 0.05; **, P < 0.01; ***, P < 0.001, by ANOVA with Tukey's test (C, E, and G). noTX, no treatment.

synergistic interaction with mSCF and VCAM-1, which are unique to mSCF in the screened factors. For instance, we did not observe any clustered patterns or morphological changes in HSCs with Ang-1, which binds to Tie2, another receptor tyrosine kinase (Arai et al., 2004). Similarly, HSCs did not form clusters with delta-1 (DLL1; Fig. 1 B), a Notch ligand reported to support the expansion of hematopoietic progenitors in an immobilized, but not soluble, form in vitro (Varnum-Finney et al., 2003). Our findings also coincide with reports on the dispensable roles of Ang-1 and Notch signaling in HSC maintenance in vivo (Varnum-Finney et al., 2011; Zhou et al., 2015). Clustering may thus play an important functional role in the membrane-bound signaling in the stem cell niche. Microcluster formation is central to the activation of T and B lymphocytes (Carrasco et al., 2004; Grakoui et al., 1999). Whereas T cells or B cells cluster T cell receptor or B cell receptor into a bullseye shape in the

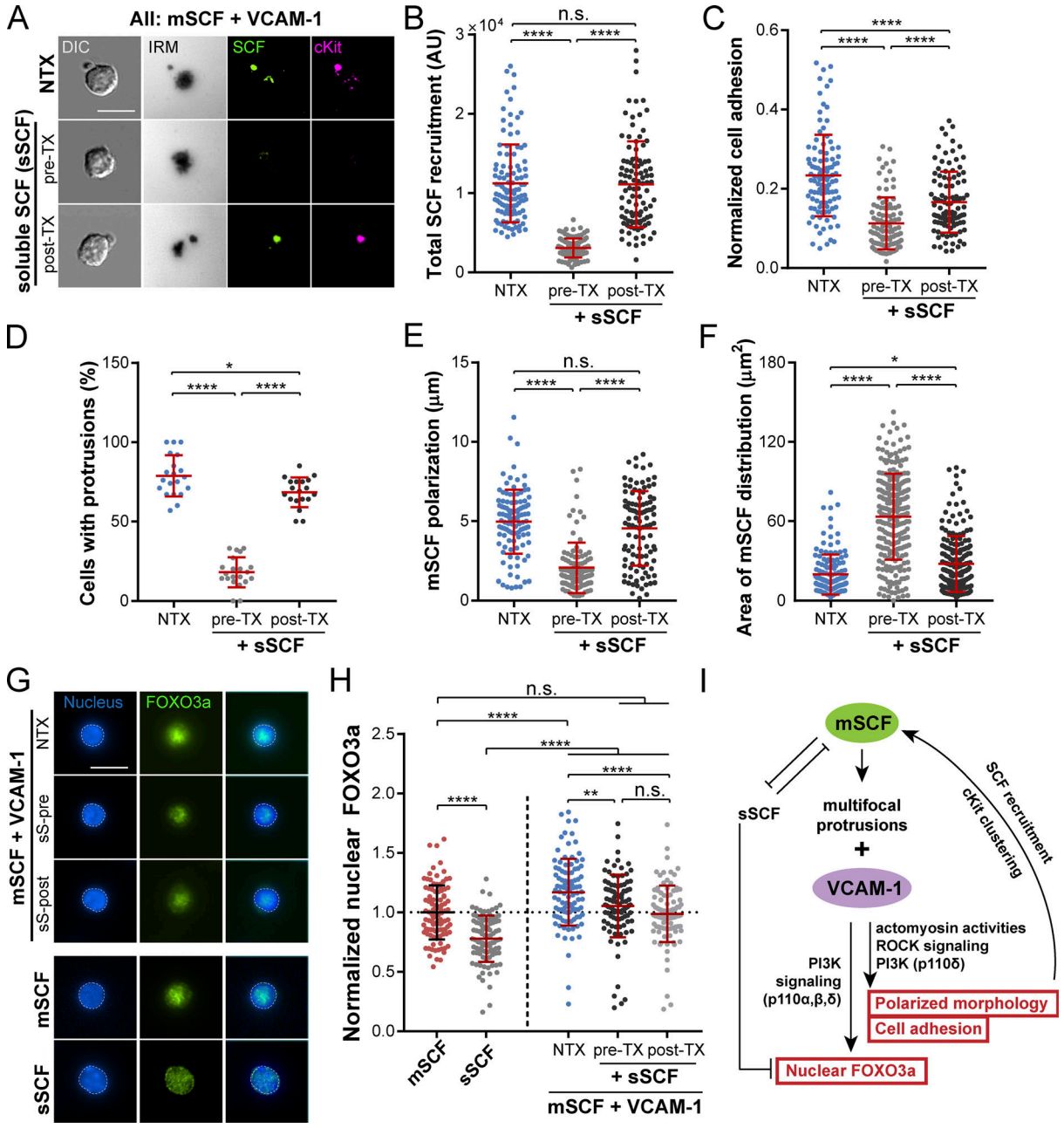

Figure 8. **sSCF competitively disrupts mSCF–VCAM-1 synergy. (A)** HSCs incubated on SLBs with mSCF+VCAM-1 for 1 h. pre-TX, pretreated with 50 ng/ml sSCF on ice for 1 h (no washing) before loading onto SLB; post-TX, HSCs allowed to interact with SLB for 30 min before being treated with 50 ng/ml sSCF for 30 min. The total interaction time with SLBs was 1 h in all conditions. **(B–F)** Corresponding quantifications of total recruited mSCF by each cell (B; *n* = 103–109 single cells per condition), normalized cell adhesion (C; *n* = 100–104 single cells per condition), frequency of cells showing large membrane protrusions (in DIC; D; *n* = 19–21 images per condition with 6–23 cells per image), polarity of mSCF distribution (E; *n* = 105–107 single cells per condition), and area of mSCF distribution (F; *n* = 100 single cells per condition). **(G)** HSCs immunostained for FOXO3a (nuclei counterstained) after 12-h incubation on SLBs. **(H)** Intensities of nuclear FOXO3a immunostaining in single HSCs, normalized to the population average of the mSCF-alone condition. *n* = 100 single cells per condition. **(I)** Summarized mechanism of mSCF–VCAM-1 synergy and regulation of HSC morphology, adhesion, and nuclear FOXO3a. Scale bars, 10 μm. Error bars represent SD. n.s., P > 0.05; *, P < 0.05; **, P < 0.01; ****, P < 0.0001 by ANOVA with Tukey's test (B–F and H). NTX, no treatment.

presence of ICAM-1, HSCs form a polarized morphology and pattern of cKit/mSCF clusters with VCAM-1, suggesting a distinct role of mSCF/cKit microclusters in HSCs from those in lymphocyte activations. Notably, all the cKit-expressing HSPCs examined in the study can form mSCF microclusters. In vivo, HSC niches are likely accessible to all the cKit⁺ HSPC populations (Christodoulou et al., 2020; Zhang et al., 2021). The mSCF recruitment by cKit may thus be a common route of HSPC–stromal interactions. Interestingly, the cKit⁺ populations (HSCs, MPPs, and OPPs) have varying efficiency in mSCF clustering (Fig. 2). As a receptor tyrosine kinase, this efficiency may indicate the strength of the cKit signaling. That being said, cKit is

upstream of several signaling pathways that involve multiple functions including cell proliferation, survival and differentiation (Lennartsson and Rönnstrand, 2012). As such, the recruitment efficiency can have different functional implications, which warrants further investigation.

Most strikingly, the polarized morphology in response to mSCF+VCAM-1 is specific to HSCs among all the HSPCs, including the closely related MPPs (MPP^- and MPP^+; Fig. 2 B). Moreover, in our SLB model, the mSCF–VCAM-1 synergy drastically increases the strength of HSC adhesion to a level that is ∼10-fold that of MPPs, whereas the protrusion provides additional adhesive strength (Fig. 4, E–G). The synergy and specificity to HSCs provide a potential cellular mechanism for the selectivity of bone marrow niche to recruit and anchor HSCs over other $cKit^+$ progenitors during HSC homing or transplantation. Conversely, disrupting the mSCF–VCAM-1 synergy may disproportionally affect the retention of HSCs in their niches more than their progenitor counterparts. In fact, such differential effect between HSCs and $cKit^+$ MPPs has been indirectly noted before, where a partial loss of cKit function led to more depletion of HSCs than MPPs in the bone marrow (Thorén et al., 2008). Our results here thus suggest a functional role of the mSCF–VCAM-1 synergy and the resultant HSC morphology in HSC homing/anchorage in the bone marrow niche. The findings and microfluidic tools may also be applied to enrich HSCs and study their heterogeneities. Additionally, while previous studies have suggested a functional role of immobilized or stromal mSCF in supporting HSC maintenance and expansion in vitro (Ajami et al., 2019; Mahadik et al., 2015), these studies were done with a mixture of HSCs and progenitors and thus do not explain the specific impact of mSCF on HSCs. The role of VCAM-1 in HSC expansion, on the other hand, has only been implied by coated fibronectin (Wilkinson et al., 2019). Our data suggest a unique effect of the mSCF–VCAM-1 synergy and importance of ligand mobility on the functions of HSCs, but not the progenitors. It will thus be important to further explore the functional consequences of the mSCF–VCAM-1 synergy on HSCs in terms of their maintenance, differentiation, and engraftment in vitro and/or in vivo.

The membrane protrusions and the morphological transformation are among the most prominent features of HSCs under the mSCF–VCAM-1 synergy. It has been reported that isolated mouse HSCs exhibit surface microspikes, and soluble cytokines such as CXCL12 and SCF can further induce the formation of membrane extensions or podia that point toward stromal cells in culture (Frimberger et al., 2001). Interestingly, these podia only exist on the motile HSCs in vitro or those lodged in peripheral organs (except bone marrow) upon transplantation in vivo, but not on those adhered to stromal cells (in vitro) or homed to bone marrow (Frimberger et al., 2001). The membrane protrusions we observed resemble these microspikes and/or podia but under the distinct context of membrane-bound HSC–stromal interactions, which has not been described in mouse HSCs before. The existence of long podia has also been seen in human $CD34^+$ HPCs in culture (Francis et al., 1998; Wagner et al., 2004). Notably, the more primitive fraction of human $CD34^+/CD38^-$ HPCs has a higher frequency of polarized morphology (Wagner et al., 2004), and these cells seek contact with a mouse stromal cell line (AFT024) through protrusions (Wagner et al., 2005). However, unlike the mouse HSCs, the polarized human HPC morphology seems to precede and is only slightly promoted by direct contact with stromal cells (Wagner et al., 2005). It was unclear whether the difference is due to the progenitors in the much less purified HPC pool than the mouse HSCs. We foresee that the SLB model can be adapted to elucidate the regulation of human HSC morphology by the molecules found in human HPC–stromal contact (Wagner et al., 2007), as well as mSCF and VCAM-1. Interestingly, HSCs formed the polarized morphology in a nonpolarized ligand field on SLBs. Similarly, T cells can spontaneously break and reestablish the symmetry of immunological synapse on a uniform SLB through the opposing effects of protein kinase C theta and Wiskott–Aldrich syndrome protein (Sims et al., 2007). Neutrophils can also self-organize into a polarized shape in uniform chemoattractant concentrations (Hind et al., 2016). Our cytoskeleton and PI3K inhibition data also suggest that the HSC polarization on SLBs is due to the intrinsic signaling of HSCs in response to mSCF and VCAM-1. Meanwhile, some intracellular molecules are distributed in a polarized manner in HSCs. Cdc42 and tubulin have been found asymmetrically distributed in HSCs from young mouse (Florian et al., 2012). We have previously observed a polarized distribution of metabolic coenzymes NAD(P)H in the freshly isolated HSCs (Zhou et al., 2020). These molecules may also play a role in regulating HSC morphology.

Another key question is regarding the nature of the protrusion. In leukocytes, membrane protrusions are often found associated with cell polarity and migration, which can be a protruding structure at the leading edge (a pseudopod) or a contractile structure at the rear (a uropod). The two structures differ in cytoskeletal composition; pseudopods are enriched with newly synthesized actin, and uropods are composed of contractile actin–myosin complexes (Sánchez-Madrid and Serrador, 2009; Xu et al., 2003). While studies on HSC morphologies are relatively few, researchers have described the microspikes or protrusions of mouse HSCs or human HPCs with various terms (e.g., magnupodia, tenupodia, proteopodia, and uropods), which resemble morphological and functional features of pseudopods and/or uropods (Francis et al., 1998; Frimberger et al., 2001; Wagner et al., 2005). However, little is known about the cytoskeletal nature of these structures and the signaling components that regulate them in HSCs. We showed that the protrusions formed by HSCs on mSCF+VCAM-1 SLBs are enriched for myosin II and F-actin, and their formation is highly dependent on new actin polymerization, myosin contraction, and ROCK signaling (Fig. 5). Therefore, they have some characteristics of pseudopods (the enriched F-actin and dependence on its polymerization; Husson et al., 2011) but share more similarity with uropods in shape and myosin II localization (Sánchez-Madrid and Serrador, 2009). However, even though cells can migrate on SLBs (Sims et al., 2007), we did not observe obvious migratory behaviors in HSCs in the study. Instead, the protrusions provide strong adhesion that resists high shear stresses (Fig. 4 E). Therefore, they may endow HSCs niche-anchoring abilities instead of migratory functions seen with a typical uropod in motile leukocytes. Yet, it is still possible that the protrusions

may play a role in migration under other contexts (e.g., chemotaxis and extravasation; Hyun et al., 2012).

The importance of VLA-4–VCAM-1 interaction in HSPC and leukocyte adhesion has been reported previously. VCAM-1 can synergize with B cell receptor for tight adhesion and enhanced signaling (Carrasco and Batista, 2006). Human HPCs adhere to stromal cells mainly through VLA4–VCAM-1 (Oostendorp and Dörmer, 1997). In mouse, this interaction is required for the homing of HSPCs to the bone marrow, but not to spleen (Vermeulen et al., 1998). Conversely, down-regulation or functional blockade of VLA4 or VCAM-1 or conditional deletion of α4 integrin result in mobilization of HPCs into the blood circulation (Qin et al., 2006; Scott et al., 2003). In our SLB model, VCAM-1 slightly increases the cell adhesion area underneath the cell body (Fig. S3, C and D) and provides a baseline adhesive strength to HSCs and MPPs (Fig. 4, E and F). However, compared with cell adhesion, we observed a more prominent role of VCAM-1 in supporting mSCF/cKit recruitment, polarization of HSC morphology, and synergistic up-regulation of HSC adhesion strength with mSCF. Indeed, anti-VLA4/VCAM-1–induced HSC mobilization is dependent on mSCF-mediated cKit signaling (Papayannopoulou et al., 1998). Our results thus support a central role of the mSCF–VCAM-1 synergy in the homing and retention of HSCs in the bone marrow niche, which may provide alternative strategies in HSC transplantation by strengthening or weakening the synergy.

Our study demonstrated a crucial role of PI3K in the mSCF–VCAM-1 synergy. Consistent with our in vitro results, PI3K activity has been implicated in HSC migration and bone marrow homing in vivo (Buitenhuis, 2011). However, PI3K is known to have many downstream targets, some of which may have opposing roles under different contexts. For example, activation of the PI3K–Akt pathway in response to growth factor stimulation (e.g., sSCF) inhibits nuclear FOXO3a in HSCs (Yamazaki et al., 2006). In contrast, our study shows a central role of PI3K in mediating the mSCF–VCAM-1 synergy, which promotes nuclear FOXO3a in HSCs in an Akt-independent manner (Fig. 7 A). It was recently reported in epithelial cells that PI3K can promote glycolysis through actin cytoskeletal remodeling in an Akt-insensitive manner (Hu et al., 2016). Since glycolysis is a key feature of quiescent HSCs (Takubo et al., 2013), and we have shown an involvement of actin cytoskeletal remodeling in mSCF–VCAM-1 synergy, we postulate that the PI3K–actin pathway may be responsible for the FOXO3a nuclear retention in our model, which will be investigated in future studies.

Among the three isoforms (p110α, p110β, and p110δ) of the class IA PI3Ks in hematopoietic cells, p110α and p110β have been reported to have redundant or dispensable roles in HSC self-renewal (Gritsman et al., 2014; Hemmati et al., 2019). Our results indicate that p110α and p110β are involved in HSC adhesion on mSCF+VCAM-1 SLBs, but their roles in redistributing mSCF clusters into a polarized form are dispensable. In contrast, inhibiting p110δ can recapitulate most of the effects on these features from pan-PI3K inhibitions (Fig. 6, H–J), highlighting the importance of p110δ in HSC–niche interactions. Interestingly, PI3Kδ inhibitors combined with antibody therapies have shown promising effects on chronic lymphocytic leukemia by releasing leukemic cells from their protective niches in the bone marrow (Brown, 2016). It is thus crucial to understand the similarity and differences in the roles of membrane-bound factors and PI3K isoforms between normal HSCs and leukemic cells to inform and improve niche-targeted leukemia treatments. Surprisingly, the maintenance of nuclear FOXO3a is only significantly disrupted by the two pan-PI3K inhibitors, but not the isoform-specific ones (Fig. 7 G), suggesting more functional redundancy of the three isoforms in the downstream nuclear signaling than cell adhesion/morphology. It also indicates the divergent roles of PI3K in regulating HSC maintenance versus adhesion/morphology downstream of the mSCF–VCAM-1 synergy (Fig. 8 I).

sSCF and mSCF have previously been shown to have diametric roles in HSCs; sSCF induces HSC proliferation (Zhang and Lodish, 2008) while mSCF is required for long-term HSC maintenance (Barker, 1994). It has been unclear, however, how HSCs receive and interpret the two signals to balance proliferation versus quiescence in the bone marrow niche. We show that sSCF competes with mSCF by disrupting cKit clustering and HSC morphology, whereas the temporal order of the two SCF forms makes a significant difference (Fig. 8, B–F). On the other hand, levels of nuclear FOXO3a remained higher in HSCs treated with both sSCF and mSCF+VCAM-1 than in those treated with sSCF alone, suggesting a more dominant role of mSCF in maintaining HSC quiescence. Overall, our results suggest a stabilizing role of mSCF in HSC retention/maintenance in the bone marrow niche. mSCF and sSCF competition may also toggle the activation between the PI3K–Akt–mTOR and PI3K–actin pathways, leading to mitochondrial respiration or glycolysis, respectively (Hu et al., 2016; Kalaitzidis et al., 2012), which also differentially regulate HSC activation or quiescence (Takubo et al., 2013).

Materials and methods

Mice

C57BL/6J mice were purchased from Jackson Laboratories. All mice were bred at the Research Animal Facility of the University of Southern California. Animal care and euthanasia protocols were approved by the Institutional Animal Care and Use Committee of the University of Southern California. Mice were provided continuously with sterile food, water, and bedding.

Cell isolation and flow cytometry

Bone marrow cells were obtained from the crushed bones of ∼4- to 6-mo-old mice and immunostained and sorted for Lin^+CD45^+ cells (BMLs) or magnetically enriched by cKit and then immunostained for HSCs, MPPs, and OPPs (Fig. S2 A). Bone marrow mesenchymal stromal cells were harvested from mouse bone marrow (Ding et al., 2012), immunostained, negatively enriched ($CD45^-$, $TER119^-$) using EasySep mouse mesenchymal stem/progenitor cell enrichment kit following vendor's instructions (catalog no. 19771; StemCell Technologies), and sorted based on PDGFRα expression. FACS sorting was performed with a BD FACS Aria II cell sorter (BD Biosciences) at 4°C.

Quantitative PCR

The phenotypic identity of the stromal cells was confirmed by their high expression of SCF (Kit ligand), CXCL12, VCAM-1, and PDGFRα using TaqMan real-time PCR assays following the vendor's instructions. Assay ID numbers are as follows: SCF, Mm00442972_m1; VCAM-1, Mm01320970_m1; CXCL12, Mm00445553_m1; LepR, Mm00440181_m1; PDGFRα, Mm00440701_m1; CD31, Mm01242576_m1), and β-actin. Mm02619580_g1).

Fabrication of lipid bilayer and cell loading chambers

The loading chambers for lipid bilayer and cells were manufactured by pouring polydimethylsiloxane (PDMS) mixed at 10:1 base to curing agent ratio (Sylgard 184 elastomer kit; Dow Corning) into a custom-milled polycarbonate mold with a rectangular plateau of 1.5 mm (width) × 6 mm (length) × 1 mm (height) raised from a flat-bottom surface. PDMS was cured at 80°C for 3 h, peeled off, and cut into individual devices. Circular inlet and outlet with a 2-mm diameter were punched at both ends of the PDMS chamber. Glass coverslips (24 mm × 40 mm; Fisher Scientific) were cleaned with piranha solution (36 M H_2SO_4:30% H_2O_2 = 3:1, by volume), extensively rinsed with deionized water, baked overnight at 400°C, and treated with plasma for 5 min before being permanently bound with PDMS chamber (model PDC-001-HP; Harrick Plasma). The PDMS chambers were treated with plasma for 50 s and permanently bound to the plasma-treated glass coverslips for the subsequent lipid bilayer formation.

Preparation of small unilamellar vesicles and SLBs

Lipid components (18:1 [Δ9-Cis] 1,2-dioleoyl-sn-glycero-3-phosphocholine [DOPC], 18:1 1,2-dioleoyl-sn-glycero-3-phospho-L-serine [DOPS], 18:1 DGS-NTA[Ni], and 18:1 Biotinyl-Cap-PE) dissolved in chloroform were purchased from Avanti Polar Lipids and mixed at mol % indicated in the main text. The lipids were dried in round-bottom flasks under a stream of N_2 for 5 min and desiccated for 2 h with house vacuum pump in a chemical fume hood. The lipid mixture was resuspended by bath sonication in 1X PBS at a final concentration of 2.5 mg/ml and extruded 10 times through a membrane with 50-nm pore size (Avanti Polar Lipids) into small unilamellar vesicles. The small unilamellar vesicle solutions were then diluted 1:1 in 1X PBS (pH 7.4) before being loaded onto the glass coverslip through the loading chamber, and incubated for 2 min to spontaneously form the lipid bilayers. The chambers were then washed with a 10X excess volume of 1X PBS. For SEM, indium-tin-oxide–coated coverslips (SPI Supplies) were used to form lipid bilayers, where DOPC was replaced with 18:1 phospho-L-serine (Kumar et al., 2009).

Protein capturing on lipid bilayer

DOPC lipids supplemented with 0.1 mol % Biotinyl-Cap-PE and 5 mol % DGS-NTA(Ni) were used to form SLBs. The bilayer was blocked with 0.1 mg/ml BSA for 1 h and incubated with 10 µg/ml streptavidin for 20 min. The bilayer was then washed extensively with PBS (pH 7.4) followed by 30-min incubation with the Alexa Fluor 488–labeled mono-biotinylated protein (5 µg/ml CXCL12, 7 µg/ml SCF, 7 µg/ml FMS-like tyrosine kinase 3 ligand, 15 µg/ml TPO, 20 µg/ml Ang-1, and 20 µg/ml DLL1; Peprotech) and DAPI/Cy5–labeled VCAM-1 with a 6-histidine tail (2 µg/ml; R&D Systems). The entire chamber was then washed with 10X excess volumes of 1X PBS. FRAP techniques were used to examine the lateral mobility, and the diffusion coefficients of the captured proteins were calculated through a custom-fitting program in MATLAB (MathWorks) using fast-Fourier transform analysis of the time evolution of the lateral fluorescence profile (Shen et al., 2009).

Cell seeding and incubation

FACS-sorted cells were kept in PBS with 2% FBS on ice. Before being seeded onto bilayers, cells were pelleted at 300×*g* and resuspended in either extracellular buffer (130 mM NaCl, 5 mM KCl, 1.5 mM $CaCl_2$, 1 mM $MgCl_2$, 25 mM Hepes, 1 mg/ml BSA, and 5 mM glucose, pH 7.4) or StemSpan SFEM (StemCell Technologies). The chamber containing lipid bilayers was equilibrated with the same buffer, and the resuspended cells were then injected into the chamber and incubated for 1 h in a humidified incubator maintained at 37°C and 5% CO_2.

Fluorescence microscopy

A Nikon Eclipse Ti-E inverted fluorescence microscope (Nikon) was used for live-cell imaging, which is equipped with an OKOLab incubation box controlling for temperature (37°C) and CO_2 concentration (5%). The chamber containing lipid bilayers was equilibrated with extracellular buffer, and the resuspended cells were then injected and live imaged on the prewarmed fluorescence microscope. IRM was used to visualize the adhesion–substratum interface of cells as described previously (Barr and Bunnell, 2009). Images were taken with a Hamamatsu Flash LT camera (C11440-42U) and Nikon Element software using a 60× 1.40 NA oil objective. In live-cell tracking and motility analysis, cells were using a 10× 0.45 NA air objective, at 5-min intervals, for 1 h.

TIRF microscopy

TIRF microscopy was performed on a DeltaVision OMX system equipped with Ring TIRF illumination optics (GE Healthcare) using a 100× 1.49 NA oil TIRF objective. Laser wavelengths of 405 nm (for F-actin), 488 nm (for mSCF), and 642 nm (for cKit) were used for excitation, and the images were collected at the emission wavelengths of 442/30 nm, 532/56 nm, and 683/40 nm, respectively.

SEM

Cell samples were fixed with 4% PFA in 1X PBS, serially dehydrated with ethanol (10%, 25%, 50%, 70%, 80%, 95, 100%, and 100%; 5 min at each concentration), critical-point dried with a Tousimis 815 Critical Point Dryer, and sputter coated with Pt:Pd for 90 s using sputter coater 108 (Cressington Scientific Instruments) to reach a thickness of 3 nm. The SEM images were acquired on a Nova NanoSEM 450 (FEI). Settings used for imaging were voltage at 3 kV, spot size at 3.5 nm, and working distance at 10.0 mm. Beam deceleration mode with a 200-V bias voltage were used to reduce the charging effect. Micrographs were taken with 6-µs scanning time at 12,000× magnification.

For angled images, samples were tilted at 45° and imaged with the same settings.

Shear flow and adhesion analysis

We created the microfluidic device in-house using a micromilling platform, design and fabrication protocols, and soft-lithography techniques (Yen et al., 2016) for shear flow and adhesion analysis. Within each device, SLBs were formed in two geometrically identical (mirrored), parallel microfluidic channels separated by a 250-µm barrier (Fig. 4 A, inset). The design and toolpaths for the double channel microdevice (channel height 1 mm, channel width 2 mm, length 16 mm) were created in Autodesk Fusion 360 and custom-milled (Carbide 3D; Shapeoko) out of polycarbonate. The final device was manufactured by pouring PDMS mixed at 10:1 base to curing agent ratio (Sylgard 184 elastomer kit; Dow Corning). PDMS was cured at 80°C for 3 h, peeled off, and cut into individual devices. Channel inlets and outlets with 0.75-mm diameter were punched at both ends of microfluidic channels. The PDMS devices were permanently bound to the detergent-cleaned glass coverslips after plasma treatment for 50 s (model PDC-001-HP; Harrick Plasma) for the subsequent lipid bilayer formation and substrate modification.

A dual-channel syringe pump (New Era Pump Systems) was used to apply controlled shear flow to the two channels through 5-ml glass syringes (inner diameter, 10.3 mm) and tubing connections. Cells were incubated with membrane-bound factors on SLBs for 1 h before infusing StemSpan SFEM media at controlled flow rates (ramping up from 0 to 15 ml/min, with 5-s holding of each flow rates in a stepwise fashion) under a 37°C environment. The design enables real-time imaging and direct comparison of cell adhesion on two different SLBs under the same flow rates. BF images were taken once every second using a 2× objective (CFI60 Plan Apochromat Lambda Lens, NA 0.1, Working Distance 8.5 mm). The remaining cells under each flow rate were normalized as a percentage by the starting cell numbers in the same regions of interest (ROIs). Each ROI is a 300 × 300–µm square containing 50–100 cells randomly selected along the center of the channel. Shear stress at the SLB surface (bottom of channel) was calculated at https://www.elveflow.com/microfluidic-calculator/, where the fluidic properties were assumed the same as water at 37°C considering the serum-free nature of the StemSpan media. For morphological analysis under flow, cells were imaged with a 60× 1.40 NA oil objective.

Treatments with inhibitors

Cells were treated with BIO 5192 (20 nM, 45 min; R&D Systems) to inhibit the VLA-4 integrin; latrunculin A (1 µM, 1 h; Tocris Bioscience) to inhibit actin polymerization; Blebb (50 µM, 10 min; MedChemExpress) to inhibit nonmuscle myosin II; Y-27632 dihydrochloride (10 µM, 1 h; Tocris Bioscience) to inhibit ROCK signaling; LY (5 µM, 1 h; MedChemExpress), BAY (Copanlisib; 64 nM, 1 h), CAL-101 (Idelalisib; 50 nM, 1 h), MLN1117 (Serabelisib; 150 nM, 1 h), and TGX-221 (85 nM, 1 h) to inhibit PI3K; and MK (5 µM, 1 h; MedChemExpress) and GSK2141795 (1 µM, 1 h) to inhibit Akt activity. Vehicle solvents were used accordingly as controls.

Immunofluorescence staining

For the detection of phosphorylated tyrosine, phosphorylated Akt, or FOXO3a, cells were fixed with 4% PFA, permeabilized with 0.2% Triton X-100 in PBS for 15 min, and blocked with 1% BSA in PBS for 1 h. 1 mM sodium orthovanadate was added throughout the fixation and staining process for phosphorylation staining. Cells were then incubated overnight at 4°C with primary antibodies in PBS with 1% BSA. On the following day, cells were rinsed extensively and incubated for 2 h at room temperature with secondary antibodies in PBS with 1% BSA. Primary antibodies are listed in Table S1. F-actin was visualized with Alexa Fluor Plus 405 Phalloidin (Invitrogen). Myosin IIa or IIb was visualized with myosin IIa antibody (3C7; catalog no. H00004627-M01; NovusBio) and myosin IIb antibody (D8H8; catalog no. 8824; Cell Signaling). Cell nucleus was visualized with DAPI staining. The Alexa Fluor 405–, 488–, or 568–conjugated goat anti-mouse, donkey anti-rabbit, and donkey anti-mouse secondary antibodies were purchased from Invitrogen.

Image analysis

Images were analyzed using ImageJ (U.S. National Institutes of Health; http://rsb.info.nih.gov/ij) supplemented with customized macro codes, including clustering parameters, adhesion, cell size, and fluorescence intensity (mean cluster intensity after background subtraction) from images taken with identical optical configurations and exposure settings. Colocalization was quantified as Pearson's correlation coefficient of pixel intensities between two images, measured with an ImageJ plugin, Coloc2.

Statistics

The HSC–LepR$^+$ MSC co-culture experiment was repeated twice. All other experiments were repeated at least three times. All data are presented in mean ± SD. *n* represents cell number analyzed in each experiment, as detailed in the figure legends. Statistical analyses and plot generation were performed using GraphPad Prism 8 software (GraphPad Software). Statistical significance was assessed using the Welch's *t* test (parametric) and Mann–Whitney (nonparametric) for pairwise comparison and ordinary one-way ANOVA for comparison among multiple (three or more) conditions. Data distribution was assumed to be normal, but this was not formally tested (N.D., not detected; n.s., $P > 0.05$; *, $P < 0.05$; **, $P < 0.01$; ***, $P < 0.001$; ****, $P < 0.0001$).

Online supplemental material

Fig. S1 shows the measurement of diffusion coefficients of membrane-bound factors on SLBs with FRAP and interpretation of ligand density by fluorescence intensity. Fig. S2 shows the FACS gating schemes for HSPCs and niche stromal cells used in the study. Fig. S3 shows the maintenance of HSC morphology over longer cultures and the role of VCAM-1 in HSC adhesion. Fig. S4 shows the dynamic regulation of mSCF clustering and HSC adhesion by VCAM-1 on SLBs and the different adhesive behavior of HSCs on immobilized SCF and VCAM-1. Fig. S5 shows the responses of HSC adhesion and SCF recruitment to drug treatments. Table S1 shows antibodies used for immunofluorescence staining.

Acknowledgments

We thank Dr. Nogalska for animal colony maintenance during the study, the USC Stem Cell Flow Cytometry Core for assistance with cell sorting, and Dr. John Curulli and Rene Zeto at USC Core Center of Excellence in Nano Imaging for providing access to and guidance on GE DeltaVision OMX and TIRF imaging.

This work was supported by the National Institutes of Health (grants R21EB024748 and R01CA220012), the University of Southern California Viterbi School of Engineering, an Eli and Edythe Broad Center of Regenerative Medicine and Stem Cell Research Innovation Award, a Rose Hills Foundation fellowship, a STOP CANCER Marni Levine Memorial Research Career Development Award, the Phi Beta Psi Charity Trust, and the University of Southern California Provost's PhD Fellowship. This research was also supported by shared resources from a National Institutes of Health National Cancer Institute Award (P30CA014089).

The authors declare no competing financial interests.

Author contributions: K. Shen conceived the project. J. Hao and K. Shen designed the study, performed data analysis and interpretation, and wrote and edited the manuscript. J. Hao performed most of the experiments. H. Zhou, D. Yen, W. Zhao, C. Bramlett, and B. Wang assisted in animal work and cell isolation. K. Nemes and D. Yen assisted in SLB experiments. R. Lu assisted in data interpretation and manuscript revision.

Submitted: 20 October 2020
Revised: 29 June 2021
Accepted: 29 July 2021

References

Acar, M., K.S. Kocherlakota, M.M. Murphy, J.G. Peyer, H. Oguro, C.N. Inra, C. Jaiyeola, Z. Zhao, K. Luby-Phelps, and S.J. Morrison. 2015. Deep imaging of bone marrow shows non-dividing stem cells are mainly perisinusoidal. *Nature.* 526:126–130. https://doi.org/10.1038/nature15250

Ajami, M., M. Soleimani, S. Abroun, and A. Atashi. 2019. Comparison of cord blood CD34 + stem cell expansion in coculture with mesenchymal stem cells overexpressing SDF-1 and soluble/membrane isoforms of SCF. *J. Cell. Biochem.* 120:15297–15309. https://doi.org/10.1002/jcb.28797

Alexeev, V., and K. Yoon. 2006. Distinctive role of the cKit receptor tyrosine kinase signaling in mammalian melanocytes. *J. Invest. Dermatol.* 126: 1102–1110. https://doi.org/10.1038/sj.jid.5700125

Arai, F., A. Hirao, M. Ohmura, H. Sato, S. Matsuoka, K. Takubo, K. Ito, G.Y. Koh, and T. Suda. 2004. Tie2/angiopoietin-1 signaling regulates hematopoietic stem cell quiescence in the bone marrow niche. *Cell.* 118: 149–161. https://doi.org/10.1016/j.cell.2004.07.004

Barker, J.E. 1994. Sl/Sld hematopoietic progenitors are deficient in situ. *Exp. Hematol.* 22:174–177.

Barr, V.A., and S.C. Bunnell. 2009. Interference reflection microscopy. *Curr. Protoc. Cell Biol.* 45:4–23. . https://doi.org/10.1002/0471143030.cb0423s45

Bilanges, B., Y. Posor, and B. Vanhaesebroeck. 2019. PI3K isoforms in cell signalling and vesicle trafficking. *Nat. Rev. Mol. Cell Biol.* 20:515–534. https://doi.org/10.1038/s41580-019-0129-z

Brown, J.R. 2016. The PI3K pathway: clinical inhibition in chronic lymphocytic leukemia. *Semin. Oncol.* 43:260–264. https://doi.org/10.1053/j.seminoncol.2016.02.004

Buitenhuis, M. 2011. The role of PI3K/protein kinase B (PKB/c-akt) in migration and homing of hematopoietic stem and progenitor cells. *Curr. Opin. Hematol.* 18:226–230. https://doi.org/10.1097/MOH.0b013e32834760e5

Caplan, A.I. 2015. Are All Adult Stem Cells The Same? *Regen. Eng. Transl. Med.* 1:4–10. https://doi.org/10.1007/s40883-015-0001-4

Carrasco, Y.R., and F.D. Batista. 2006. B-cell activation by membrane-bound antigens is facilitated by the interaction of VLA-4 with VCAM-1. *EMBO J.* 25:889–899. https://doi.org/10.1038/sj.emboj.7600944

Carrasco, Y.R., S.J. Fleire, T. Cameron, M.L. Dustin, and F.D. Batista. 2004. LFA-1/ICAM-1 interaction lowers the threshold of B cell activation by facilitating B cell adhesion and synapse formation. *Immunity.* 20: 589–599. https://doi.org/10.1016/S1074-7613(04)00105-0

Chen, S., M. Lewallen, and T. Xie. 2013. Adhesion in the stem cell niche: biological roles and regulation. *Development.* 140:255–265. https://doi.org/10.1242/dev.083139

Christodoulou, C., J.A. Spencer, S.A. Yeh, R. Turcotte, K.D. Kokkaliaris, R. Panero, A. Ramos, G. Guo, N. Seyedhassantehrani, T.V. Esipova, et al. 2020. Live-animal imaging of native haematopoietic stem and progenitor cells. *Nature.* 578:278–283. https://doi.org/10.1038/s41586-020-1971-z

Crane, G.M., E. Jeffery, and S.J. Morrison. 2017. Adult haematopoietic stem cell niches. *Nat. Rev. Immunol.* 17:573–590. https://doi.org/10.1038/nri.2017.53

Cuchiara, M.L., K.L. Horter, O.A. Banda, and J.L. West. 2013. Covalent immobilization of stem cell factor and stromal derived factor 1α for in vitro culture of hematopoietic progenitor cells. *Acta Biomater.* 9:9258–9269. https://doi.org/10.1016/j.actbio.2013.08.012

Decker, M., J. Leslie, Q. Liu, and L. Ding. 2018. Hepatic thrombopoietin is required for bone marrow hematopoietic stem cell maintenance. *Science.* 360:106–110. https://doi.org/10.1126/science.aap8861

Ding, L., T.L. Saunders, G. Enikolopov, and S.J. Morrison. 2012. Endothelial and perivascular cells maintain haematopoietic stem cells. *Nature.* 481: 457–462. https://doi.org/10.1038/nature10783

Dittmann, A., T. Werner, C.-W. Chung, M.M. Savitski, M. Fälth Savitski, P. Grandi, C. Hopf, M. Lindon, G. Neubauer, R.K. Prinjha, et al. 2014. The commonly used PI3-kinase probe LY294002 is an inhibitor of BET bromodomains. *ACS Chem. Biol.* 9:495–502. https://doi.org/10.1021/cb400789e

Driessen, R.L., H.M. Johnston, and S.K. Nilsson. 2003. Membrane-bound stem cell factor is a key regulator in the initial lodgment of stem cells within the endosteal marrow region. *Exp. Hematol.* 31:1284–1291. https://doi.org/10.1016/j.exphem.2003.08.015

Dustin, M.L. 2007. Cell adhesion molecules and actin cytoskeleton at immune synapses and kinapses. *Curr. Opin. Cell Biol.* 19:529–533. https://doi.org/10.1016/j.ceb.2007.08.003

Eaves, C., C. Miller, J. Cashman, E. Conneally, A. Petzer, P. Zandstra, and A. Eaves. 1997. Hematopoietic stem cells: inferences from in vivo assays. *Stem Cells.* 15(S2, Suppl 1):1–5. https://doi.org/10.1002/stem.5530150802

Edidin, M. 2003. Lipids on the frontier: a century of cell-membrane bilayers. *Nat. Rev. Mol. Cell Biol.* 4:414–418. https://doi.org/10.1038/nrm1102

Ehninger, A., and A. Trumpp. 2011. The bone marrow stem cell niche grows up: mesenchymal stem cells and macrophages move in. *J. Exp. Med.* 208: 421–428. https://doi.org/10.1084/jem.20110132

Feng, Q., C. Chai, X.S. Jiang, K.W. Leong, and H.Q. Mao. 2006. Expansion of engrafting human hematopoietic stem/progenitor cells in three-dimensional scaffolds with surface-immobilized fibronectin. *J. Biomed. Mater. Res. A.* 78:781–791. https://doi.org/10.1002/jbm.a.30829

Ferraro, F., C.L. Celso, and D. Scadden. 2010. Adult stem cels and their niches. *Adv. Exp. Med. Biol.* 695:155–168. https://doi.org/10.1007/978-1-4419-7037-4_11

Florian, M.C., K. Dörr, A. Niebel, D. Daria, H. Schrezenmeier, M. Rojewski, M.-D. Filippi, A. Hasenberg, M. Gunzer, K. Scharffetter-Kochanek, et al. 2012. Cdc42 activity regulates hematopoietic stem cell aging and rejuvenation. *Cell Stem Cell.* 10:520–530. https://doi.org/10.1016/j.stem.2012.04.007

Fonseca, A.V., D. Freund, M. Bornhäuser, and D. Corbeil. 2010. Polarization and migration of hematopoietic stem and progenitor cells rely on the RhoA/ROCK I pathway and an active reorganization of the microtubule network. *J. Biol. Chem.* 285:31661–31671. https://doi.org/10.1074/jbc.M110.145037

Francis, K., R. Ramakrishna, W. Holloway, and B.O. Palsson. 1998. Two new pseudopod morphologies displayed by the human hematopoietic KG1a progenitor cell line and by primary human CD34(+) cells. *Blood.* 92: 3616–3623. https://doi.org/10.1182/blood.V92.10.3616

Frimberger, A.E., C.I. McAuliffe, K.A. Werme, R.A. Tuft, K.E. Fogarty, B.O. Benoit, M.S. Dooner, and P.J. Quesenberry. 2001. The fleet feet of haematopoietic stem cells: rapid motility, interaction and proteopodia. *Br. J. Haematol.* 112:644–654. https://doi.org/10.1046/j.1365-2141.2001.02542.x

Grakoui, A., S.K. Bromley, C. Sumen, M.M. Davis, A.S. Shaw, P.M. Allen, and M.L. Dustin. 1999. The immunological synapse: a molecular machine controlling T cell activation. *Science.* 285:221–227. https://doi.org/10.1126/science.285.5425.221

Gritsman, K., H. Yuzugullu, T. Von, H. Yan, L. Clayton, C. Fritsch, S.-M. Maira, G. Hollingworth, C. Choi, T. Khandan, et al. 2014. Hematopoiesis and RAS-driven myeloid leukemia differentially require PI3K isoform p110α. *J. Clin. Invest.* 124:1794–1809. https://doi.org/10.1172/JCI69927

Hemmati, S., T. Sinclair, M. Tong, B. Bartholdy, R.O. Okabe, K. Ames, L. Ostrodka, T. Haque, I. Kaur, T.S. Mills, et al. 2019. PI3 kinase alpha and delta promote hematopoietic stem cell activation. *JCI Insight.* 5:e125832. https://doi.org/10.1172/jci.insight.125832

Hind, L.E., W.J.B. Vincent, and A. Huttenlocher. 2016. Leading from the Back: The Role of the Uropod in Neutrophil Polarization and Migration. *Dev. Cell.* 38:161–169. https://doi.org/10.1016/j.devcel.2016.06.031

Horiuchi, K., H. Morioka, H. Takaishi, H. Akiyama, C.P. Blobel, and Y. Toyama. 2009. Ectodomain shedding of FLT3 ligand is mediated by TNF-alpha converting enzyme. *J. Immunol.* 182:7408–7414.

Hu, H., A. Juvekar, C.A. Lyssiotis, E.C. Lien, J.G. Albeck, D. Oh, G. Varma, Y.P. Hung, S. Ullas, J. Lauring, et al. 2016. Phosphoinositide 3-Kinase Regulates Glycolysis through Mobilization of Aldolase from the Actin Cytoskeleton. *Cell.* 164:433–446. https://doi.org/10.1016/j.cell.2015.12.042

Husson, J., K. Chemin, A. Bohineust, C. Hivroz, and N. Henry. 2011. Force generation upon T cell receptor engagement. *PLoS One.* 6:e19680. https://doi.org/10.1371/journal.pone.0019680

Hyun, Y.M., R. Sumagin, P.P. Sarangi, E. Lomakina, M.G. Overstreet, C.M. Baker, D.J. Fowell, R.E. Waugh, I.H. Sarelius, and M. Kim. 2012. Uropod elongation is a common final step in leukocyte extravasation through inflamed vessels. *J. Exp. Med.* 209:1349–1362. https://doi.org/10.1084/jem.20111426

Jacobsen, K., J. Kravitz, P.W. Kincade, and D.G. Osmond. 1996. Adhesion receptors on bone marrow stromal cells: in vivo expression of vascular cell adhesion molecule-1 by reticular cells and sinusoidal endothelium in normal and gamma-irradiated mice. *Blood.* 87:73–82. https://doi.org/10.1182/blood.V87.1.73.73

Jing, D., A.V. Fonseca, N. Alakel, F.A. Fierro, K. Muller, M. Bornhauser, G. Ehninger, D. Corbeil, and R. Ordemann. 2010. Hematopoietic stem cells in co-culture with mesenchymal stromal cells--modeling the niche compartments in vitro. *Haematologica.* 95:542–550. https://doi.org/10.3324/haematol.2009.010736

Kalaitzidis, D., S.M. Sykes, Z. Wang, N. Punt, Y. Tang, C. Ragu, A.U. Sinha, S.W. Lane, A.L. Souza, C.B. Clish, et al. 2012. mTOR complex 1 plays critical roles in hematopoiesis and Pten-loss-evoked leukemogenesis. *Cell Stem Cell.* 11:429–439. https://doi.org/10.1016/j.stem.2012.06.009

Kollet, O., A. Dar, S. Shivtiel, A. Kalinkovich, K. Lapid, Y. Sztainberg, M. Tesio, R.M. Samstein, P. Goichberg, A. Spiegel, et al. 2006. Osteoclasts degrade endosteal components and promote mobilization of hematopoietic progenitor cells. *Nat. Med.* 12:657–664. https://doi.org/10.1038/nm1417

Kumar, K., C.S. Tang, F.F. Rossetti, M. Textor, B. Keller, J. Vörös, and E. Reimhult. 2009. Formation of supported lipid bilayers on indium tin oxide for dynamically-patterned membrane-functionalized microelectrode arrays. *Lab Chip.* 9:718–725. https://doi.org/10.1039/B814281E

Lane, S.W., D.A. Williams, and F.M. Watt. 2014. Modulating the stem cell niche for tissue regeneration. *Nat. Biotechnol.* 32:795–803. https://doi.org/10.1038/nbt.2978

Lennartsson, J., and L. Rönnstrand. 2012. Stem cell factor receptor/c-Kit: from basic science to clinical implications. *Physiol. Rev.* 92:1619–1649. https://doi.org/10.1152/physrev.00046.2011

Li, D., W. Xue, M. Li, M. Dong, J. Wang, X. Wang, X. Li, K. Chen, W. Zhang, S. Wu, et al. 2018. VCAM-1^{+} macrophages guide the homing of HSPCs to a vascular niche. *Nature.* 564:119–124. https://doi.org/10.1038/s41586-018-0709-7

Liu, J., C. Sato, M. Cerletti, and A. Wagers. 2010. Notch signaling in the regulation of stem cell self-renewal and differentiation. *Curr. Top Dev. Biol.* 92:367–409. https://doi.org/10.1016/S0070-2153(10)92012-7

Mahadik, B.P., S. Pedron Haba, L.J. Skertich, and B.A.C. Harley. 2015. The use of covalently immobilized stem cell factor to selectively affect hematopoietic stem cell activity within a gelatin hydrogel. *Biomaterials.* 67:297–307. https://doi.org/10.1016/j.biomaterials.2015.07.042

Manz, B.N., and J.T. Groves. 2010. Spatial organization and signal transduction at intercellular junctions. *Nat. Rev. Mol. Cell Biol.* 11:342–352. https://doi.org/10.1038/nrm2883

Matsunaga, T., N. Takemoto, T. Sato, R. Takimoto, I. Tanaka, A. Fujimi, T. Akiyama, H. Kuroda, Y. Kawano, M. Kobune, et al. 2003. Interaction between leukemic-cell VLA-4 and stromal fibronectin is a decisive factor for minimal residual disease of acute myelogenous leukemia. *Nat. Med.* 9:1158–1165. https://doi.org/10.1038/nm909

Mazzoldi, E.L., S. Pavan, G. Pilotto, K. Leone, A. Pagotto, S. Frezzini, M.O. Nicoletto, A. Amadori, and A. Pastò. 2019. A juxtacrine/paracrine loop between C-Kit and stem cell factor promotes cancer stem cell survival in epithelial ovarian cancer. *Cell Death Dis.* 10:412. https://doi.org/10.1038/s41419-019-1656-4

Miyamoto, K., K.Y. Araki, K. Naka, F. Arai, K. Takubo, S. Yamazaki, S. Matsuoka, T. Miyamoto, K. Ito, M. Ohmura, et al. 2007. Foxo3a is essential for maintenance of the hematopoietic stem cell pool. *Cell Stem Cell.* 1:101–112. https://doi.org/10.1016/j.stem.2007.02.001

Morrison, S.J., and D.T. Scadden. 2014. The bone marrow niche for haematopoietic stem cells. *Nature.* 505:327–334. https://doi.org/10.1038/nature12984

Oostendorp, R.A., and P. Dörmer. 1997. VLA-4-mediated interactions between normal human hematopoietic progenitors and stromal cells. *Leuk. Lymphoma.* 24:423–435. https://doi.org/10.3109/10428199709055581

Papayannopoulou, T., C. Craddock, B. Nakamoto, G.V. Priestley, and N.S. Wolf. 1995. The VLA4/VCAM-1 adhesion pathway defines contrasting mechanisms of lodgement of transplanted murine hemopoietic progenitors between bone marrow and spleen. *Proc. Natl. Acad. Sci. USA.* 92:9647–9651. https://doi.org/10.1073/pnas.92.21.9647

Papayannopoulou, T., G.V. Priestley, and B. Nakamoto. 1998. Anti-VLA4/VCAM-1-induced mobilization requires cooperative signaling through the kit/mkit ligand pathway. *Blood.* 91:2231–2239. https://doi.org/10.1182/blood.V91.7.2231

Qin, G., M. Ii, M. Silver, A. Wecker, E. Bord, H. Ma, M. Gavin, D.A. Goukassian, Y.S. Yoon, T. Papayannopoulou, et al. 2006. Functional disruption of α4 integrin mobilizes bone marrow-derived endothelial progenitors and augments ischemic neovascularization. *J. Exp. Med.* 203:153–163. https://doi.org/10.1084/jem.20050459

Sánchez-Madrid, F., and J.M. Serrador. 2009. Bringing up the rear: defining the roles of the uropod. *Nat. Rev. Mol. Cell Biol.* 10:353–359. https://doi.org/10.1038/nrm2680

Scott, L.M., G.V. Priestley, and T. Papayannopoulou. 2003. Deletion of α4 integrins from adult hematopoietic cells reveals roles in homeostasis, regeneration, and homing. *Mol. Cell. Biol.* 23:9349–9360. https://doi.org/10.1128/MCB.23.24.9349-9360.2003

Shen, K., J. Tsai, P. Shi, and L.C. Kam. 2009. Self-aligned supported lipid bilayers for patterning the cell-substrate interface. *J. Am. Chem. Soc.* 131:13204–13205. https://doi.org/10.1021/ja904721h

Shin, J.-W., A. Buxboim, K.R. Spinler, J. Swift, D.A. Christian, C.A. Hunter, C. Léon, C. Gachet, P.C. Dingal, I.L. Ivanovska, et al. 2014a. Contractile forces sustain and polarize hematopoiesis from stem and progenitor cells. *Cell Stem Cell.* 14:81–93. https://doi.org/10.1016/j.stem.2013.10.009

Shin, J.Y., W. Hu, M. Naramura, and C.Y. Park. 2014b. High c-Kit expression identifies hematopoietic stem cells with impaired self-renewal and megakaryocytic bias. *J. Exp. Med.* 211:217–231. https://doi.org/10.1084/jem.20131128

Sims, T.N., T.J. Soos, H.S. Xenias, B. Dubin-Thaler, J.M. Hofman, J.C. Waite, T.O. Cameron, V.K. Thomas, R. Varma, C.H. Wiggins, et al. 2007. Opposing effects of PKCtheta and WASp on symmetry breaking and relocation of the immunological synapse. *Cell.* 129:773–785. https://doi.org/10.1016/j.cell.2007.03.037

Takubo, K., G. Nagamatsu, C.I. Kobayashi, A. Nakamura-Ishizu, H. Kobayashi, E. Ikeda, N. Goda, Y. Rahimi, R.S. Johnson, T. Soga, et al. 2013. Regulation of glycolysis by Pdk functions as a metabolic checkpoint for cell cycle quiescence in hematopoietic stem cells. *Cell Stem Cell.* 12:49–61. https://doi.org/10.1016/j.stem.2012.10.011

Thorén, L.A., K. Liuba, D. Bryder, J.M. Nygren, C.T. Jensen, H. Qian, J. Antonchuk, and S.E.W. Jacobsen. 2008. Kit regulates maintenance of quiescent hematopoietic stem cells. *J. Immunol.* 180:2045–2053. https://doi.org/10.4049/jimmunol.180.4.2045

Ullrich, A., and J. Schlessinger. 1990. Signal transduction by receptors with tyrosine kinase activity. *Cell.* 61:203–212. https://doi.org/10.1016/0092-8674(90)90801-K

Varnum-Finney, B., C. Brashem-Stein, and I.D. Bernstein. 2003. Combined effects of Notch signaling and cytokines induce a multiple log increase in precursors with lymphoid and myeloid reconstituting ability. *Blood.* 101:1784–1789. https://doi.org/10.1182/blood-2002-06-1862

Varnum-Finney, B., L.M. Halasz, M. Sun, T. Gridley, F. Radtke, and I.D. Bernstein. 2011. Notch2 governs the rate of generation of mouse long- and short-term repopulating stem cells. *J. Clin. Invest.* 121:1207–1216. https://doi.org/10.1172/JCI43868

Vermeulen, M., F. Le Pesteur, M.-C. Gagnerault, J.-Y. Mary, F. Sainteny, and F. Lepault. 1998. Role of adhesion molecules in the homing and mobilization of murine hematopoietic stem and progenitor cells. *Blood.* 92:894–900. https://doi.org/10.1182/blood.V92.3.894

Wagner, W., A. Ansorge, U. Wirkner, V. Eckstein, C. Schwager, J. Blake, K. Miesala, J. Selig, R. Saffrich, W. Ansorge, and A.D. Ho. 2004. Molecular

evidence for stem cell function of the slow-dividing fraction among human hematopoietic progenitor cells by genome-wide analysis. *Blood.* 104:675–686. https://doi.org/10.1182/blood-2003-10-3423

Wagner, W., R. Saffrich, U. Wirkner, V. Eckstein, J. Blake, A. Ansorge, C. Schwager, F. Wein, K. Miesala, W. Ansorge, and A.D. Ho. 2005. Hematopoietic progenitor cells and cellular microenvironment: behavioral and molecular changes upon interaction. *Stem Cells.* 23:1180–1191. https://doi.org/10.1634/stemcells.2004-0361

Wagner, W., F. Wein, C. Roderburg, R. Saffrich, A. Faber, U. Krause, M. Schubert, V. Benes, V. Eckstein, H. Maul, and A.D. Ho. 2007. Adhesion of hematopoietic progenitor cells to human mesenchymal stem cells as a model for cell-cell interaction. *Exp. Hematol.* 35:314–325. https://doi.org/10.1016/j.exphem.2006.10.003

Walasek, M.A., R. van Os, and G. de Haan. 2012. Hematopoietic stem cell expansion: challenges and opportunities. *Ann. N. Y. Acad. Sci.* 1266: 138–150. https://doi.org/10.1111/j.1749-6632.2012.06549.x

Wei, Q., and P.S. Frenette. 2018. Niches for Hematopoietic Stem Cells and Their Progeny. *Immunity.* 48:632–648. https://doi.org/10.1016/j.immuni.2018.03.024

Wilkinson, A.C., R. Ishida, M. Kikuchi, K. Sudo, M. Morita, R.V. Crisostomo, R. Yamamoto, K.M. Loh, Y. Nakamura, M. Watanabe, et al. 2019. Long-term ex vivo haematopoietic-stem-cell expansion allows nonconditioned transplantation. *Nature.* 571:117–121. https://doi.org/10.1038/s41586-019-1244-x

Xu, J., F. Wang, A. Van Keymeulen, P. Herzmark, A. Straight, K. Kelly, Y. Takuwa, N. Sugimoto, T. Mitchison, and H.R. Bourne. 2003. Divergent signals and cytoskeletal assemblies regulate self-organizing polarity in neutrophils. *Cell.* 114:201–214. https://doi.org/10.1016/S0092-8674(03)00555-5

Yamazaki, S., A. Iwama, S-i. Takayanagi, Y. Morita, Eto K., H. Ema, and H. Nakauchi. 2006. Cytokine signals modulated via lipid rafts mimic niche signals and induce hibernation in hematopoietic stem cells. *EMBO J.* 25: 3515–3523.

Yen, D.P., Y. Ando, and K. Shen. 2016. A cost-effective micromilling platform for rapid prototyping of microdevices. *Technology (Singap World Sci).* 4: 234–239. https://doi.org/10.1142/S2339547816200041

Zhang, C.C., and H.F. Lodish. 2008. Cytokines regulating hematopoietic stem cell function. *Curr. Opin. Hematol.* 15:307–311. https://doi.org/10.1097/MOH.0b013e3283007db5

Zhang, J., Q. Wu, C.B. Johnson, G. Pham, J.M. Kinder, A. Olsson, A. Slaughter, M. May, B. Weinhaus, A. D'Alessandro, et al. 2021. In situ mapping identifies distinct vascular niches for myelopoiesis. *Nature.* 590: 457–462. https://doi.org/10.1038/s41586-021-03201-2

Zhou, B.O., R. Yue, M.M. Murphy, J.G. Peyer, and S.J. Morrison. 2014. Leptin-receptor-expressing mesenchymal stromal cells represent the main source of bone formed by adult bone marrow. *Cell Stem Cell.* 15:154–168. https://doi.org/10.1016/j.stem.2014.06.008

Zhou, B.O., L. Ding, and S.J. Morrison. 2015. Hematopoietic stem and progenitor cells regulate the regeneration of their niche by secreting Angiopoietin-1. *eLife.* 4:e05521. https://doi.org/10.7554/eLife.05521

Zhou, H., L. Nguyen, C. Arnesano, Y. Ando, M. Raval, J.T. Rodgers, S. Fraser, R. Lu, and K. Shen. 2020. Non-invasive Optical Biomarkers Distinguish and Track the Metabolic Status of Single Hematopoietic Stem Cells. *iScience.* 23:100831. https://doi.org/10.1016/j.isci.2020.100831

Supplemental material

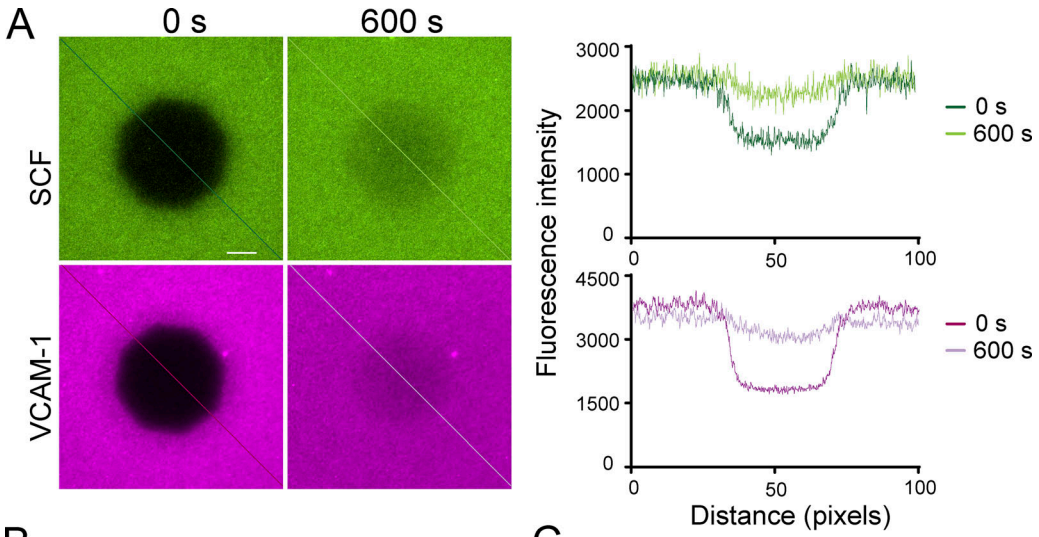

B

membrane-bound factors	diffusion coefficient mean ± SD (μm²/s)
VCAM-1	0.315 ± 0.040
SCF	0.382 ± 0.022
CXCL12	0.378 ± 0.149
Ang1	0.287 ± 0.077
DLL	0.280 ± 0.070
TPO	0.255 ± 0.084
Flt3L	0.254 ± 0.051

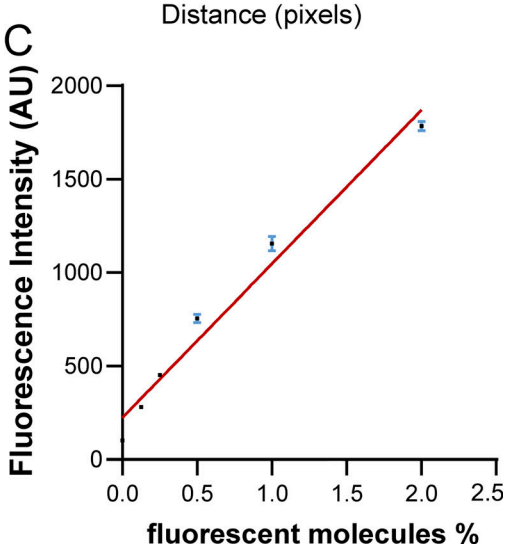

Figure S1. **Measuring diffusion coefficients of the membrane-bound factors on SLBs with FRAP. (A)** Measuring diffusion coefficients of the membrane-bound factors on supported lipid bilayers with FRAP. Green and purple show fluorescently labeled SCF and VCAM-1. Left: Right after photobleaching. Right: The same area after 600 s of recovery using the same acquisition settings. **(B)** Diffusion coefficients of membrane-bound factors measured from the FRAP experiments. **(C)** Linear relationship between fluorescence intensity of lipid bilayer and the percentage of fluorescent lipid molecules. Lipid bilayers were composed of DOPC and 0%, 0.125%, 0.25%, 0.5%, 1%, and 2% Texas Red DHPE (1,2-dihexadecanoyl-*sn*-glycero-3-phosphoethanolamine, triethylammonium salt). Error bars represent SD.

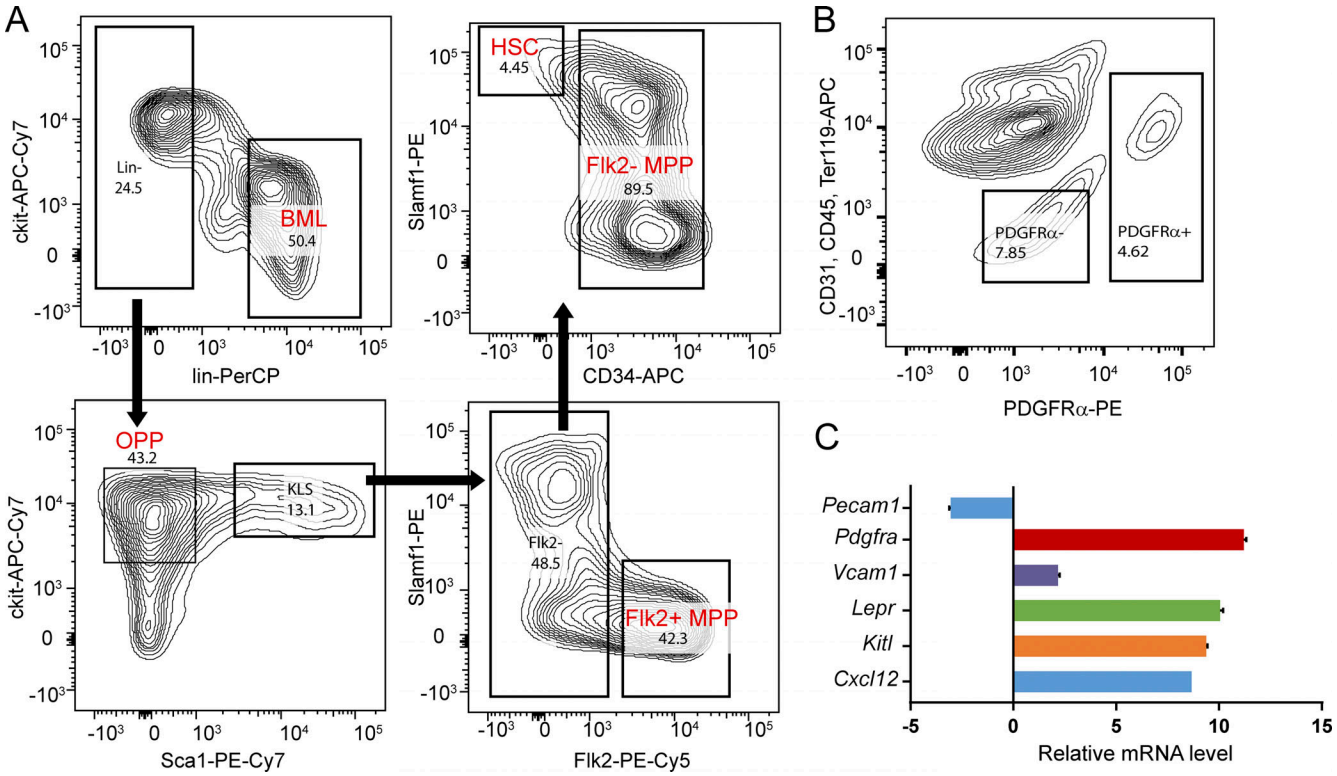

Figure S2. **Gating for hematopoietic and stromal populations from bone marrow. (A)** Gating scheme for hematopoietic populations from bone marrow. Sorting starts from DAPI⁻ singlets. Following the arrows: (a) Lin⁺ and Lin⁻ populations; (b) OPPs and cKit⁺Lin⁻Sca1⁺ cells (KLS); (c) Flk2⁺ MPPs (MPP⁺) and Flk2⁻ cells, and (d) HSCs and Flk2⁻ MPPs (MPP⁻). Lin: lineage markers, including B220, CD3, CD4, CD8, Gr1, Mac1, and Ter119. Numbers indicate the percentage of the gated populations to the parent population. **(B)** Gating scheme for niche stromal cells (LepR⁺ MSCs; PDGFα⁺ gate) and control cells (PDGFα⁻ gate). **(C)** The phenotypic identity of the stromal cells was confirmed by their high expression of SCF (Kit ligand), CXCL12, VCAM-1, and PDGFRα compared with PDGFRα-negative cells using quantitative PCR. Flow cytometer channels: PerCP (Laser 488 nm, Bandpass filter [BP] 695/40), APC (Laser 633 nm, BP 660/20) , PE-Cy7 (Laser 561 nm, BP 780/60), PE-Cy5 (Laser 561 nm, BP 670/14). PE (Laser 561 nm, BP 582/15). Error bars represent SD.

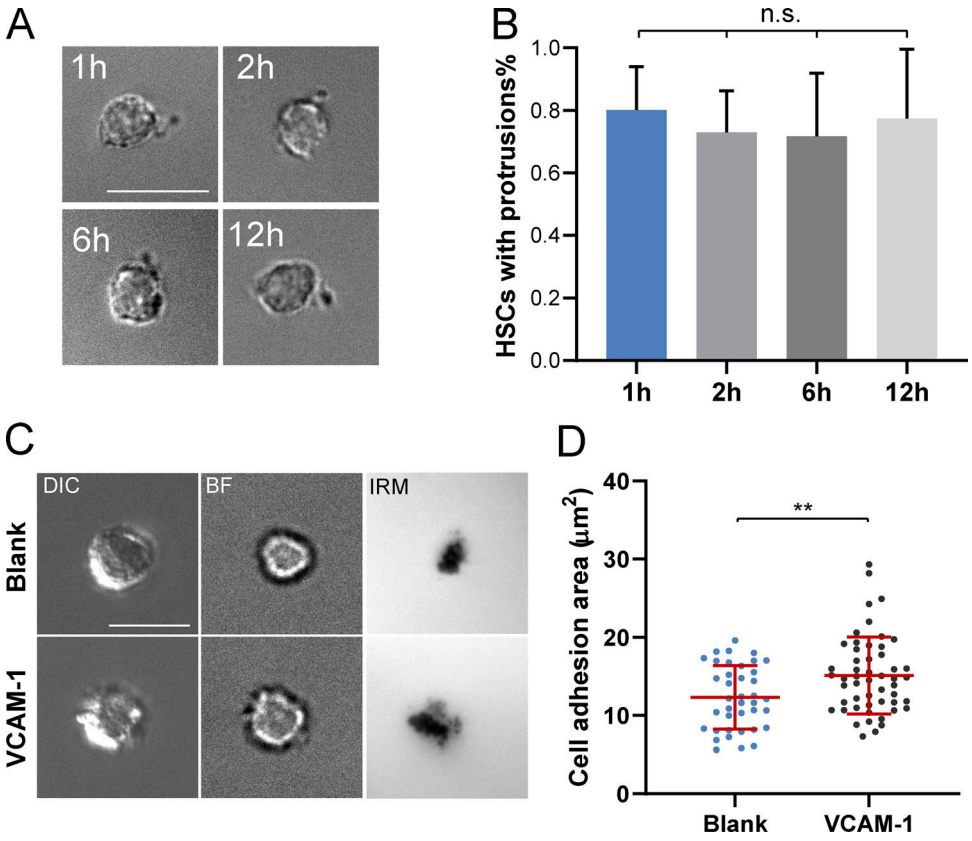

Figure S3. **Morphological maintenance of HSCs and the role of VCAM-1 in HSC adhesion. (A)** HSCs maintain polarized morphology on an SLB with mSCF+VCAM-1 at 1, 2, 6, and 12 h in the culture. **(B)** The percentages of HSCs with protrusions remain stable over 12 h. n.s., $P > 0.05$ by ANOVA and Tukey's test. **(C)** VCAM-1 promotes HSC adhesion to lipid bilayers. Representative DIC, bright-field (BF), and IRM images of HSCs incubated with a blank lipid bilayer or a lipid bilayer tethered with VCAM-1. **(D)** Quantification of cell adhesion areas measured from IRM images. $n = 39$ (blank) and 52 (VCAM-1) single cells per condition. Error bars represent SD. **, $P < 0.01$ by unpaired Student's t test (two tailed). Scale bars, 10 μm.

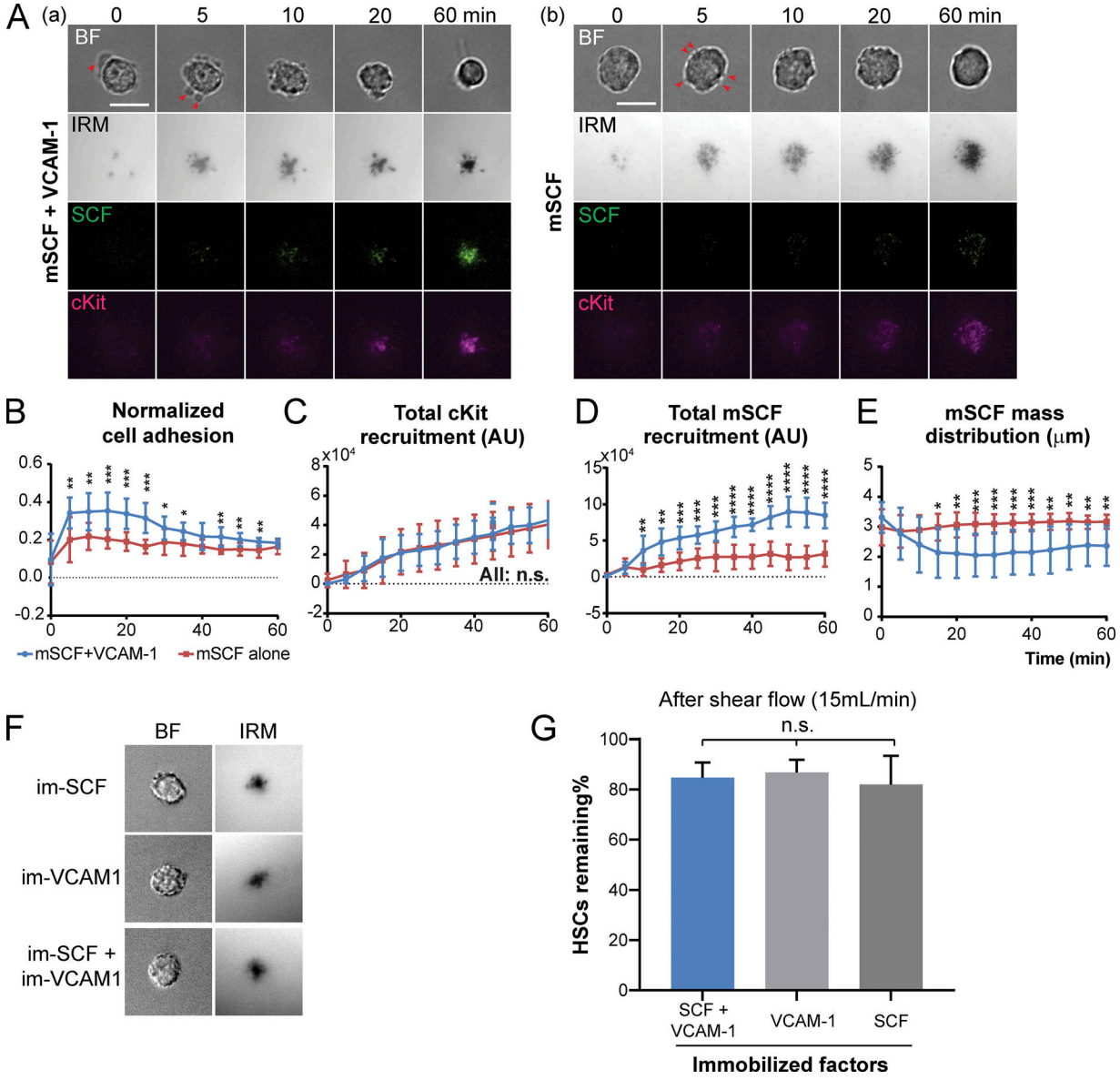

Figure S4. **Dynamic regulation of HSC–mSCF interaction by VCAM-1 and importance of lateral mobility in mSCF–VCAM-1 synergy. (A)** VCAM-1 is a dynamic regulator of HSC–mSCF interaction. Time-lapse images of HSCs seeded on supported lipid bilayers tethered with mSCF (a) with VCAM-1 or (b) without VCAM-1. **(B)** Normalized cell adhesion assessed by the dark area in IRM channel divided by cell area. **(C)** Total recruitment of cKit by HSCs assessed by the sum of fluorescence intensities of all pixels under the cells after background subtraction. **(D)** Total recruitment of mSCF by HSCs. **(E)** Mass distribution of recruited mSCF. *n* = 10 single cells per condition. *, P < 0.05; **, P < 0.01; ***, P < 0.001; ****, P < 0.0001 by Student's *t* test. Scale bar, 10 μm. **(F)** HSCs show similar morphology on coverslips with immobilized SCF, VCAM-1, or both factors. **(G)** HSCs have similar adhesion strength on the three immobilized surfaces, as indicated by the percentage of remaining HSCs after a series of shear flow up to 15 ml/min. *n* = 5 ROIs per condition. Each ROI has 50–100 HSCs. n.s., P > 0.05 by ANOVA and Tukey's test. BF, bright field.

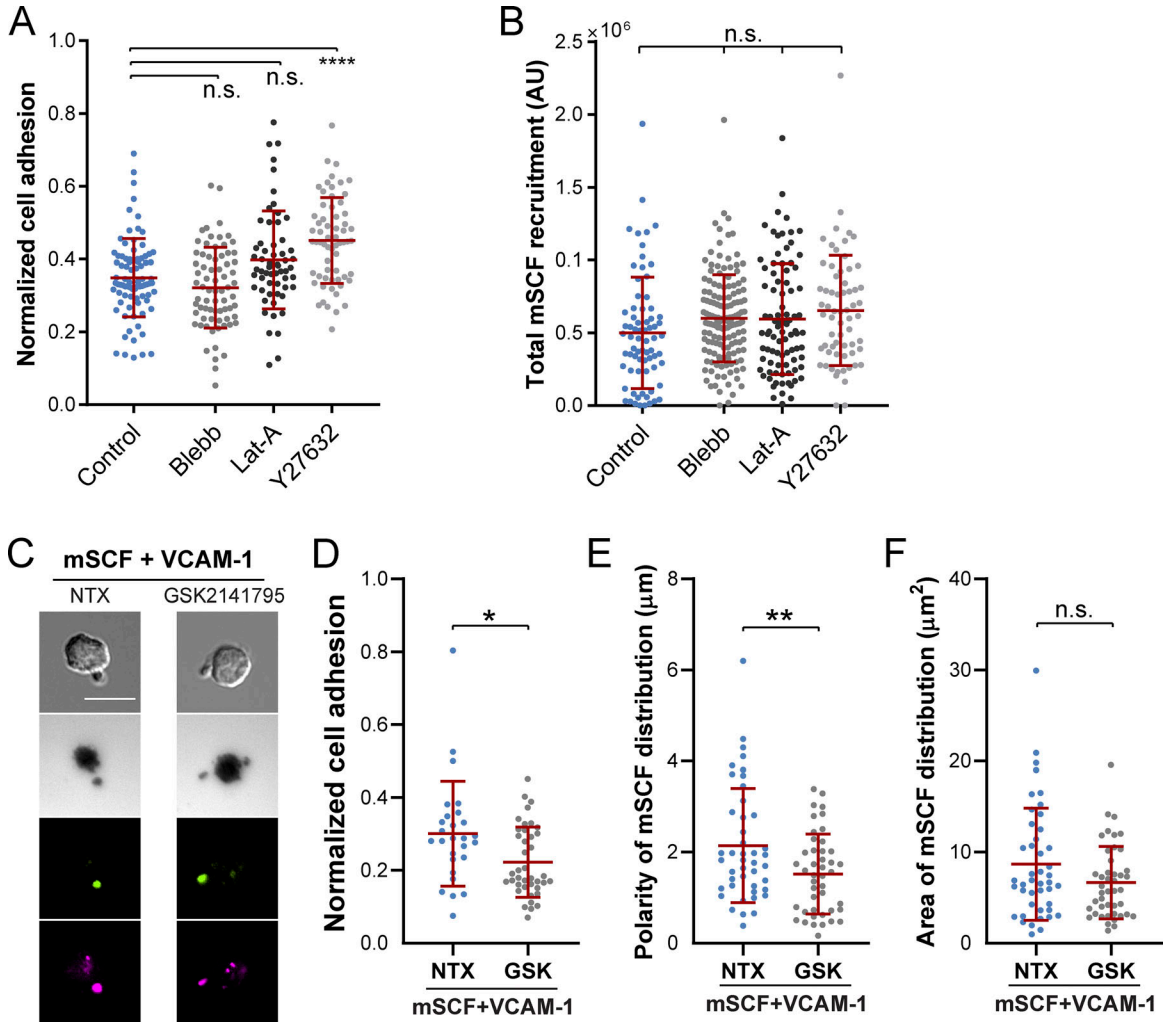

Figure S5. **Regulation of HSC adhesion and mSCF distribution by cytoskeletal and Akt inhibitors. (A)** Impact of cytoskeletal inhibition on the normalized adhesion area in HSCs, which is assessed by the dark adhesion area in IRM divided by the cell area in DIC in each cell. *n* = 59–84 single cells per condition. n.s., P > 0.05; ****, P < 0.0001 by ANOVA with Tukey's test. **(B)** None of the cytoskeletal inhibition affected the total recruitment of mSCF by HSCs assessed by the sum of fluorescence intensities of all pixels under single cells after background subtraction. *n* = 64–145 single cells per condition. **(C)** Images of HSCs on mSCF+VCAM-1 SLB without treatment (NTX) or with Akt inhibitor GSK2141795 (GSK). Scale bar, 10 μm. **(B–D)** Effect of GSK treatment on normalized cell adhesion (B), polarity of mSCF distribution (C), and area of mSCF distribution (D). n.s., P > 0.05; *, P < 0.05; **, P < 0.01 by unpaired two-tailed Student's t test.

Table S1 is provided online as a separate Word file and lists antibodies used for immunofluorescence staining.